

# X-ray evidence for multiphase hot gas with solar abundances in the brightest elliptical galaxies

David A. Buote<sup>1,2</sup>

<sup>1</sup> *UCO/Lick Observatory, University of California at Santa Cruz, Santa Cruz, CA 95064, U.S.A.*

<sup>2</sup> *Chandra Fellow*

1 June 2021

## ABSTRACT

We examine whether isothermal models of the hot gas can successfully describe the *ASCA* and *ROSAT* spectra of NGC 1399, NGC 4472, NGC 4636, and NGC 5044, which are among the brightest elliptical galaxies in X-rays. Broad-band spectral fitting of the *ASCA* SIS and GIS data accumulated within a radius of  $\sim 5'$  for each galaxy shows that isothermal models (which also include a component for discrete sources) are unable to fit the SIS data near 1 keV, although a marginal fit for NGC 4636 is obtained if the relative abundances of several elements with respect to Fe are allowed to depart substantially from their solar values. In addition, these isothermal models typically fail to produce the large equivalent widths of the  $K\alpha$  line blends of Si and S which are measured independently of the Fe L emission lines.

Two-temperature models provide substantially better broad-band fits to both the SIS and GIS data of each galaxy with the relative abundances (except for NGC 4636) fixed at their solar values. A simple multiphase cooling flow model fits nearly as well as the two-temperature model for NGC 1399, NGC 4472, and NGC 5044. The multiphase models also predict more accurately the Si and S equivalent widths and the ratios of Si XIV/XIII and S XVI/XV than the isothermal models. From detailed comparison of broad-band fits to the *ASCA* data of these ellipticals using the MEKAL and Raymond-Smith plasma codes we determine that the MEKAL plasma code (as expected) is significantly more accurate for the important energies  $\sim 0.7\text{--}1.4$  keV, and the small residuals in the Fe L region for the best-fitting multiphase models imply that remaining inaccuracies in the MEKAL code are insufficient to change qualitatively the results for data of the present quality.

Using various approaches we find that the temperature gradients inferred from the *ROSAT* PSPC data of these galaxies, especially for NGC 1399 and NGC 5044, are inconsistent with the isothermal models obtained from fitting the *ASCA* data within a single aperture but are very consistent with the multiphase models. Therefore, models which assume isothermal gas within  $r \sim 5'$  are inconsistent with the *ASCA* and *ROSAT* PSPC data of these elliptical galaxies. Simple two-temperature models and multiphase cooling flows provide much better descriptions of these data sets with Fe abundances of  $\sim 1\text{--}2$  solar and (except for NGC 4636) relative abundances fixed at their solar values. We discuss the implications of these nearly solar abundances.

**Key words:** galaxies: general – galaxies: evolution – X-rays: galaxies.

## 1 INTRODUCTION

The elemental abundances inferred from X-ray observations of elliptical galaxies are sensitive diagnostics of models of the formation and evolution of the hot gas in these systems. For example, the relative abundances of the  $\alpha$ -process elements with respect to Fe are affected by the relative contributions

of Type Ia and Type II supernovae to the enrichment of the hot gas (e.g. David, Jones, & Forman 1991). The standard models that rely on Type Ia supernova to enrich the hot gas tend to predict Fe abundances well in excess of solar (e.g. Ciotti et al. 1991). Smaller Fe abundances can be accommodated by other models (e.g. Fujita et al. 1997; Brighenti & Mathews 1998b).

Most studies of ellipticals based on X-ray spectral data from the *ASCA* satellite (Tanaka et al. 1994) find very sub-solar Fe abundances ( $\sim 0.3Z_{\odot}$ ). These low abundances are generally deduced from fitting isothermal models of the hot gas to the accumulated *ASCA* spectra within circular apertures of typical radius  $r \sim 3'-5'$ . These findings have been christened as a “Standard Model” by Loewenstein & Mushotzky (1997) who review the results obtained from the *ASCA* spectra of ellipticals.

In a recent study of the *ASCA* data of 20 bright ellipticals, Buote & Fabian (1998; hereafter BF) concluded that the spectra of the brightest galaxies in their sample require at least two temperature components in the hot gas (in addition to any possible emission from discrete sources). The multiphase models predict Fe abundances for these galaxies that are generally consistent with solar. These results for the brightest ellipticals highlight the sensitivity of the Fe abundance to the spectral model.

These results of BF also do not fit into the Standard Model and have been criticized by Loewenstein & Mushotzky (1998; also Loewenstein 1998) in two key respects. First, Loewenstein & Mushotzky state that the *ASCA* data can generally be described by two-component models consisting of one “soft” component of isothermal hot gas and another “hard” component due to discrete sources. Second, they claim that the  $K\alpha$  emission line ratios of Si XIV/XIII are very consistent with these isothermal models but are only marginally consistent with the multiphase models of BF.

In this paper we re-examine the *ASCA* data of the brightest ellipticals to address these criticisms and thus determine whether indeed isothermal models with very sub-solar Fe abundances are adequate descriptions of the X-ray spectra of elliptical galaxies. We extend the work of BF in the following respects: (1) we examine in detail the predictions of the Standard Model using two-component models where one component is isothermal hot gas and the other is a high-temperature bremsstrahlung component presumably due to discrete sources; (2) the equivalent widths and ratios of the Si and S line blends measured locally for each galaxy are used to constrain the isothermal and multiphase models obtained from broad-band analysis; and (3) we examine whether the radial temperature gradients found by studies of the *ROSAT* data of bright ellipticals are consistent with the Standard Model.

We focus our analysis on NGC 1399, NGC 4472, NGC 4636, and NGC 5044 which are among the brightest ellipticals in X-rays and have *ASCA* data with the best signal-to-noise ratios (S/N) for the sample studied by BF. Moreover, these galaxies were observed during the *ASCA* Performance-Verification (PV) phase at which time the performance of the CCDs, in particular the energy resolution, had not yet degraded from radiation damage (see Dotani et al. 1995). This is especially important for our local measurements of the Si and S lines. Data from a very deep exposure of NGC 4636 has also become available to the public. These new data for NGC 4636 have the highest S/N in our sample.

The paper is organized as follows. In section 2 we discuss the observations and reduction of the *ASCA* data. The broad-band spectral fitting is presented in detail in section 3. In section 4 we summarize our measurements of the Si and S line blends and compare them to the models obtained

from the broad-band fits. We analyze the *ROSAT* data and compare the results to the models derived from fitting the *ASCA* data in section 5. In section 6 we evaluate our results in light of the Standard Model and discuss the implications of the derived metal abundances. Finally, we present a detailed summary of our results in section 7.

## 2 *ASCA* OBSERVATIONS AND DATA REDUCTION

The *ASCA* X-ray satellite consists of four detectors: two X-ray CCD cameras (Solid State Imaging Spectrometers – SIS0 and SIS1) and two proportional counters (Gas Imaging Spectrometers – GIS2 and GIS3). Each SIS is a square array of four  $420 \times 422$  pixel CCD chips with a total field of view of  $22 \text{ arcmin}^2$ . The usable field of view of each GIS lies within a circle of radius  $20 \text{ arcmin}^2$ . Each detector is illuminated by its own X-ray telescope (XRT) consisting of 119 nested layers of thin foil. Although the point spread function (PSF) of each XRT has a relatively sharp core, the wings of the PSF are quite broad (half power diameter  $\sim 3'$ ) and increase markedly for energies above a few keV (e.g. Kunieda et al. 1995). Since the angular sizes of the elliptical galaxies in our sample are comparable to this PSF, we do not attempt to analyze the spatial distribution of the *ASCA* data of these sources. Rather, (as in most previous studies) we analyze the *ASCA* X-ray emission within a single large aperture for each galaxy which encloses most of the detectable emission; we address the spatial properties of the X-ray emission with *ROSAT* data in section 5.

We obtained *ASCA* data for NGC 1399, NGC 4472, NGC 4636, and NGC 5044 from the public data archive maintained by the High Energy Astrophysics Science Archive Research Center (HEASARC). The basic properties of these galaxies are listed in Table 1 and the observation sequence numbers are listed in Table 2. The second sequence (80026010) for NGC 5044 began 2 minutes after the first sequence (80026000) and the pointing for each sequence was identical. Since the gain and response of the detectors do not change significantly over such time scales, we directly combined the events of these two sequences. The observation sequence for NGC 4636 listed in Table 2 corresponds to the deep exposure taken in 1995. (Note that we do find that the significantly shorter PV-phase observation of NGC 4636 (see section 3.3.2) gives results that are consistent with this deep observation.)

The data were reduced with the standard FTOOLS (v4.1) software according to the procedures described in The *ASCA* Data Reduction Guide and the WWW pages of the *ASCA* Guest Observer Facility (GOF)\* For the observations of NGC 1399, NGC 4472, and NGC 5044 (all taken in the PV phase) we used the events files generated by the default screening criteria processed under the Revision 2 Data Processing (REV2). As is standard procedure for analysis of SIS data, only data in BRIGHT mode taken in medium or high bit rate were used for these galaxies. Since the NGC

\* See <http://heasarc.gsfc.nasa.gov/docs/asca/abc/abc.html> and <http://heasarc.gsfc.nasa.gov/docs/asca/>.

**Table 1.** Galaxy Properties

Name	Type	$z$	$B_T^0$	$\sigma_0$ (km s <sup>-1</sup> )	$N_H$ (10 <sup>21</sup> cm <sup>-2</sup> )	Group
NGC 1399	E1P	0.00483	10.79	310	0.13	Fornax
NGC 4472	E2	0.00290	09.32	287	0.16	Virgo
NGC 4636	E0 <sup>+</sup>	0.00365	10.50	191	0.17	Virgo
NGC 5044	E0	0.00898	11.87	234	0.50	WP 23

Morphological types and redshifts are taken from RC3. Total blue magnitudes ( $B_T^0$ ) and central velocity dispersions ( $\sigma_0$ ) are taken from Faber et al. (1989). Galactic Hydrogen column densities ( $N_H$ ) are from Stark et al. (1992).

**Table 2.** ASCA Observation Properties

Name	Sequence #	Exposure (10 <sup>3</sup> s)		Count Rate (10 <sup>-2</sup> ct s <sup>-1</sup> )		Exposure (10 <sup>3</sup> s)		Count Rate (10 <sup>-2</sup> ct s <sup>-1</sup> )	
		SIS0	SIS1	SIS0	SIS1	GIS2	GIS3	GIS2	GIS3
NGC 1399	80038000	17.0	17.6	38.0	39.1	19.6	19.6	18.7	17.9
	80039000	14.8	17.0	41.9	28.8	19.8	19.9	15.4	13.6
NGC 4472	60029000	14.3	12.5	43.8	34.0	22.7	22.7	15.4	16.0
	60030000	16.5	13.9	37.0	28.8	22.2	22.2	11.2	14.0
NGC 4636	64008000	241.2	241.4	37.0	30.0	191.2	191.2	6.4	7.7
NGC 5044	80026000 + 80026010	18.4	13.1	109.2	72.0	17.9	15.5	31.2	33.5

The exposures include any time filtering. The count rates are given for energies 0.55-9 keV for the SIS and 1-9 keV for the GIS. The count rates are background subtracted within the particular aperture (see text in section 2).

4636 observation was performed in 1995 its SIS data are degraded to some extent because of radiation damage to the CCDs (see Dotani et al. 1995).

One of the problems caused by radiation damage is the Residual Dark Distribution (RDD) which is essentially an increase in the dark current of the CCDs (see <http://www.astro.isas.ac.jp/~dotani/rdd.html>). RDD degrades the energy resolution and the detection efficiency of the data. We corrected the NGC 4636 data for this effect following the procedure outlined on the ASCA GOF WWW pages which produces corrected SIS event files in BRIGHT2 mode constructed using the default screening criteria. (Again, only data with medium or high bit rate were used.)

The gain of the SIS varies from chip-to-chip, and the variation is a function of time owing to radiation damage. We have corrected the SIS data for these effects using the most up-to-date calibration files as of this writing (sisph2pi\_110397.fits). Finally, the screened SIS and GIS events files for each galaxy were further modified by excluding time intervals of high background. We mention that no dead time corrections were required for the GIS data because the count rates were less than 1 ct s<sup>-1</sup> for each GIS detector for all the observations in Table 2.

The final processed events were then extracted from a region centered on the emission peak for each detector of each sequence. We selected a particular extraction region using the following general guidelines. Our primary concern is to select a region that encloses most of the X-ray emission yet is symmetrically distributed about the origin of the region; as a result, we used circles for most of our extraction apertures. We limited the size of the aperture to ensure that the entire aperture fit on the detector, an issue more important for the SIS because of its smaller field-of-view. Moreover, for the SIS0 and SIS1 we tried to limit the apertures to as small a number of chips as possible to reduce the effects of residual errors in chip-to-chip calibration. The

GIS regions were chosen to be of similar size to the corresponding SIS regions of a given sequence for consistency. Since, however, the GIS+XRT PSF is somewhat larger than that of the SIS+XRT the extraction regions for the GIS are usually ~ 20% larger.

We extracted the events using regions defined in detector coordinates as is recommended in the ASCA ABC GUIDE because the spectral response depends on the location in the detector not the position on the sky. (Also, this avoids the problem in the current software in handling regions defined in sky coordinates.) For the GIS data of all of the galaxies we chose circular extraction regions:  $r = 6'$  for NGC 1399 and NGC 4636 and  $r = 6.5'$  for NGC 4472 and NGC 5044. Similarly, circles were used for the SIS observations of NGC 1399 ( $r = 4.7'$ ) and NGC 5044 ( $r = 5.3'$ ); note the radius of NGC 1399 is slightly smaller to reduce contamination from NGC 1404.

For the SIS data of NGC 4472 and NGC 4636 we used apertures different from circles. The resulting extracted spectra, however, are not very sensitive to these differences in aperture shape since the S/N is lowest near the aperture boundaries where these shape differences are most pronounced. The X-ray emission of NGC 4472 is elongated (see Irwin & Sarazin 1996) and thus we used a slightly flattened ellipse for the SIS data of sequence 60029000:  $(a, b) = (4.6', 5.5')$ . The pointing of sequence 60030000 places the center closer to the edge of one of the CCDs and thus we decided a box with half-widths  $(4.2', 4.7')$  was a better choice to maximize S/N yet still be symmetrically positioned about the origin. NGC 4636 was observed in single-ccd mode and thus a box (half-width  $4.6'$ ) was used. (Note the aperture radii for the SIS are averages of the SIS0 and SIS1 radii, where the SIS1 radii are generally smaller by ~ 10% because of their lower count rates.)

We computed background spectra for each detector using the standard deep observations of blank fields. There are important advantages to using these background templates

instead of a local background estimate. First, the templates allow background to be extracted from the same parts of the detector as the source and thus the vignetting and other exposure effects are the same for each; this is not the case for background taken from a different region of the detector as the current software does not allow the required corrections to be made for spectral analysis. Second, it is known from *ROSAT* observations of these galaxies that their emission extends at least over the whole field of view of the SIS and probably more (Trinchieri et al. 1994; David et al. 1994; Rangarajan et al. 1995; Irwin & Sarazin 1996; Jones et al. 1997). This is especially important for NGC 4636 as it was observed in single-ccd mode. Also, since the background templates are created from deep exposures ( $> 100$ ks) the statistical error is much less than for local background obtained from the NGC 1399, NGC 4472, and NGC 5044 observations. However, it should be emphasized that for these sources the integrated spectra within the relatively large apertures are not dominated by background and, as a result, the deduced temperatures and abundances are hardly affected whether the templates or local background are used (e.g. Buote & Canizares 1997).

The SIS background templates we obtained from the HEASARC data archive were selected to have the same standard event screening criteria as were the events files of the galaxies in our sample. We performed the rise-time filtering (i.e. GISCLEAN) on the standard GIS templates as required to match the standard screening. In Table 2 the background-subtracted count rates for each observation in each detector are listed.

The instrument response matrix required for spectral analysis of *ASCA* data is the product of a spectral Redistribution Matrix File (RMF) and an Auxiliary Response File (ARF). The RMF specifies the channel probability distribution for a photon (i.e. energy resolution information) while the ARF contains the information on the effective area. The RMFs for the GIS2 and GIS3 are equivalent, and thus for all GIS spectra we use the GIS RMFs gis2v4.0.rmf and its twin gis3v4.0.rmf obtained from the HEASARC archive. An RMF needs to be generated specifically for each SIS of each observation because, among other reasons, each chip of each SIS requires its own RMF and the spectral resolution of the SIS is degrading with time. We generated the responses for each SIS using the FTOOL SISRMG selecting for the standard event grades (0234). Using the response matrix and spectral PI (Pulse Invariant) file we constructed an ARF file with the FTOOL ASCAARF.

The source apertures used for the SIS observations of NGC 1399, NGC 4472, and NGC 5044 overlapped more than one chip. In order to analyze the spectra of such regions we followed the standard procedure of creating a new response matrix that is the average of the individual response matrices of each chip weighted by the number of source counts of each chip (i.e. within the source aperture). (Actually, the current software only allows the RMFs to be averaged and then an ARF is generated using the averaged RMF. This is considered to be a good approximation for most sources.) Unfortunately, some energy resolution is lost as a result of this averaging. For the observations of our sources, however, this small energy broadening is rendered undetectable by the statistical noise of the data.

To maximize the S/N of our data we desire to com-

bine the spectra of all available observation sequences for a given galaxy; e.g. as in NGC 5044 above. There are two observations each for NGC 1399 and NGC 4472 taken during the PV phase. Since these observations are separated by only one day for NGC 1399 and six days for NGC 4472 the responses of each observation for each galaxy can be considered the same. However, the pointings for the consecutive observations in each case were somewhat different; e.g., the center of NGC 1399 is positioned at the midpoints of different SIS chips for each observation. Hence, we can combine the spectra of the consecutive observations for NGC 1399 and NGC 4472 and use averaged RMFs and ARFs for spectral analysis without significant loss of energy resolution. However, we do not combine the PV-phase (1993) observation of NGC 4636 (see BF) with the 1995 observation listed in Table 2 because the responses are sufficiently different to warrant separate analysis of the data.

To further improve the S/N we also consider combining the spectra from each SIS and similarly for each GIS; i.e.  $SIS = SIS0 + SIS1$  and  $GIS = GIS2 + GIS3$ . For the GIS data this does not result in significant loss of information because the RMFs of the GIS2 and GIS3 are the same and time-independent; only the ARFs need to be averaged for the GIS2 and GIS3. However, the responses of the SIS0 and SIS1 detectors are different and thus the required averaging of the RMFs and ARFs leads again to loss of information. Because the gain in S/N is important for our study, we examine the combined SIS and combined GIS data of each galaxy where all of the sequences listed in Table 2 for a given galaxy have been summed. For each galaxy the source spectra, RMF, ARF, and background for each detector of each observation are summed and scaled appropriately using the FTOOL ADDASCASPEC (v1.27).

Overall we found that the results obtained from analysis of these summed SIS spectra agree well with results obtained without summing the data. We mention below (section 3.3.1) the instances where differences in the SIS0 and SIS1 data are significant.

### 3 BROAD-BAND SPECTRAL FITTING OF *ASCA* DATA

We begin our interpretation of the *ASCA* data by fitting models to the broad-band spectra of each galaxy. For the SIS data we examine energies 0.55-9 keV and for the GIS 1-9 keV. The cutoff at 9 keV is chosen because at higher energies calibration errors are significant (Gendreau & Yaqoob 1997), and the background dominates the signal (thus amplifying any error in the background level). The low energy cutoffs are dictated by calibration uncertainties (see *ASCA* GOF WWW pages).

Since the X-ray emission of the ellipticals in our sample is dominated by hot gas, we use coronal plasma models as our basic component. We focus on the MEKAL code which is a modification of the original MEKA code (Mewe, Gronenschild, & van den Oord 1985; Kaastra & Mewe 1993) where the Fe L shell transitions crucial to the X-ray emission of ellipticals have been re-calculated (Liedahl et. al 1995). For comparison, we also use the Raymond-Smith code (RS) (Raymond & Smith 1977). Although the RS code does not include the updated Fe L calculations, nor does it include



ing larger group sizes (i.e. 50 and 100 counts) but found no qualitative differences in the best-fitting models.

The normalizations of all model components are fitted separately for each data set. For example, when jointly fitting multicomponent models to the summed SIS and summed GIS data the normalizations of each model component for the SIS and GIS are free parameters. This is done to account for differences in the SIS and GIS fluxes due to small region size differences and gain differences between the detectors. A side-effect of this procedure is that in some instances the relative normalizations of the model components for the SIS can differ qualitatively from those of the GIS. We discuss these occurrences below. (All of this also applies to joint fitting of SIS0 and SIS1 data and/or GIS2 and GIS3 data.)

The procedure we follow for spectral fitting is similar to that described in BF. That is, we begin by fitting a single MEKAL model modified by Galactic absorption (Stark et al. 1992) where the relative abundances of the elements with respect to Fe are fixed at their solar values; i.e. the free parameters are the temperature, metallicity, and normalization. We then examine whether allowing  $N_{\text{H}}$  to be free significantly improves the fit; note that any excess absorption so detected is only an estimate of absorbing material intrinsic to the galaxy in question (see BF).

We proceed to add other components, one at a time, until all free parameters of consequence have been varied. We focus on the following combinations of “thermal+discrete” models where each component is modified by its own absorption: (1) 1T + BREM, (2) 2T, (3) 2T + BREM, (4) CF+1T, (5) CF+1T+BREM. (Models having more components do not significantly improve the fits to the ASCA data.) For multicomponent models with BREM we restricted the absorption on the BREM component to be its Galactic value since the emission from discrete sources is not expected to suffer from excess absorption. (At any rate, we did not find much improvement in the fits when allowing the BREM absorption to be a free parameter.) The cooling flow models (4) and (5) account for gas that is not participating in the cooling flow by adding a component of isothermal gas to the CF model where the temperature of the isothermal component is tied to the maximum temperature of the cooling flow component; e.g. our generic cooling flow model (4) can be expressed as  $\text{phabs} \times \text{CF} + \text{phabs} \times \text{MEKAL}$ , where “phabs” represents the photo-electric absorption on each component and  $T_{\text{MEKAL}} = T_{\text{CF}}$ .

Initially, the relative abundances with respect to Fe of any MEKAL/RS components are fixed at their solar values; i.e. the Fe abundance is the only abundance which is initially a free parameter. Once the best-fit versions of models (1)-(5) have been found, we then investigate allowing the relative abundances of other elements to be free. We typically allow the abundances of the following  $\alpha$ -process elements, one at a time, to be free parameters: Si, S, Ar, Mg, Ne, O. However, we do examine whether allowing the abundances of other elements can improve the fits of various models. For multicomponent models the abundance of a particular element in one component is tied to the corresponding value in the other component. (Relaxing this restriction did not noticeably improve the fits in any case.)

We emphasize that to achieve the global minimum for the multicomponent models often requires some effort (see

BF). Often the fits land in a local minimum upon first adding another component to a model. To help correct this problem, after a fit is completed we always reset a subset of the free parameters and fit again several times until we are satisfied that the minimum is stable. Stepping through the parameters when determining confidence limits also was useful in assessing the stability of the minimum. This is not the most rigorous method to find the global minimum, but it is at present the most convenient way to do it in XSPEC.

### 3.1 Relative importance of SIS and GIS

It is important to understand how much the SIS and GIS detectors modify an incident galaxy spectrum in order to interpret the spectral fitting results in the next section. For this discussion we consider a MEKAL plasma with a temperature of 1 keV, solar abundances, and a redshift and an emission measure similar to the galaxies in our sample. This model is plotted in Figure 1.

The most striking features of the plasma are the emission lines, particularly the complex of Fe L shell lines around 1 keV. These Fe L lines are generally the strongest and most temperature sensitive lines for elliptical galaxies. Other prominent lines involve  $K\alpha$  transitions of O, Mg, Si, S, and Ar. These lines individually tend not to be as sensitive as Fe L to the plasma temperature, but in tandem are very useful for probing the plasma emission measure distribution. We refer the reader to Buote et al. (1998) for a discussion of the temperature sensitivity of these lines for models of elliptical galaxies.

Much of the information provided by these lines is lost when folded through the responses of the SIS and GIS detectors. However, the degradation in the folded data is far from equal in the two cases. In Figure 1 we plot the 1 keV plasma model folded through the SIS and GIS responses. For the sake of visual clarity the folded spectrum of each detector is shown separately. We also provide a separate panel in Figure 1 showing both the SIS and GIS spectra to facilitate visual comparison of the effective area as a function of energy of the detectors.

The superior energy resolution of the SIS allows the He-like and H-like  $K\alpha$  line blends of Si and S to be clearly resolved (though S XVI  $\text{ly-}\alpha$  is weak). In contrast, these He-like and H-like line complexes are unresolved by the GIS; i.e. only the blends of the combined He-like and H-like  $K\alpha$  lines are apparent. Significant structure of the Fe L complex, though unresolved, is readily apparent in the SIS unlike the GIS.

Given the importance of the Fe L lines and the other emission lines around 2-3 keV, it is significant that the count rate of the SIS is larger than the GIS, particularly near 1 keV where the ratio of count rates is  $\sim 5 : 1$ . In fact, the count rate of the GIS only exceeds the SIS for energies above  $\sim 7$  keV where the count rate is very low in both detectors.

Considering as well that the GIS does not have reliable data below  $\lesssim 0.8$  keV where there is significant Fe L emission, it is clear that for elliptical galaxies the SIS data possess much more information than the GIS data and thus the SIS provides the most important constraints on the temperatures and abundances of these systems. These properties must be kept in mind when assessing the quality of the spectral fits to which we now turn our attention.

### 3.2 Quality of fits: isothermal vs multiphase models

In this section we address our primary objective to determine whether broad-band fits to the *ASCA* spectra using models consisting of a single temperature component of hot gas and a bremsstrahlung component representing discrete sources (i.e. 1T+BREM) are of comparable quality to fits consisting of at least two temperature components of hot gas (i.e. 2T, 2T+BREM, CF+1T, and CF+1T+BREM). The quality of the fits and the general properties of the best-fitting parameters are examined in this section. We defer detailed discussion of the derived model parameters to section 3.3.

Whereas BF emphasized joint fitting of the SIS0 and SIS1 data for each available observation, we focus on analysis of the total summed SIS data fitted jointly to the summed GIS data (see end of section 2). In addition to the gain in S/N offered by using the summed data (which is also important for studying individual lines – see section 4), the spectral analysis and presentation is simplified greatly since only two spectra (i.e. the total SIS and GIS) need to be simultaneously modeled for each galaxy. We discuss the reliability of using the summed data sets in section 3.3.1 below.

In Table 3 we list the  $\chi^2$  values and null hypothesis probabilities ( $P$ ) for the best-fitting models of each galaxy fitted jointly to the summed SIS and summed GIS data. We plot in Figures 2, 3, and 4 a subset of the best-fitting models listed in Table 3 for NGC 1399. The Fe abundance is a free parameter in all of the fits. Results where relative abundances of the elements with respect to Fe are either held fixed at their solar values (fix) or allowed to vary (var) are presented for the 1T+BREM and 2T+BREM models; the 2T model with variable relative abundances is not displayed because the values of the derived abundances and the improvement in  $\chi^2$  are very similar to the 2T+BREM model in all cases. Only fixed relative abundance results are given for the cooling flow models because the current implementation of the cooling flow model does not allow for variable relative abundances owing to prohibitive computational expense.

#### 3.2.1 MEKAL models

Let us consider the joint fits to the SIS and GIS data where the MEKAL plasma code is used for the model components of hot gas, and let us presently focus on the models with fixed relative abundances. Examination of Table 3 reveals that NGC 1399, NGC 4472, and NGC 5044 behave quite similarly when fitted by the models shown. The 1T+BREM models are strongly excluded ( $P \ll 1$ ) for all of the galaxies. From examination of the residuals in Figure 2 it is clear that the poor fits of the 1T+BREM models are mostly the result of the SIS data in the Fe L energy region  $\sim 0.7$  keV - 1.4 keV.

If instead of the 1T+BREM model we consider a model with two plasma temperature components (i.e. 2T model) we find that the fits for NGC 1399, NGC 4472, and NGC 5044 are substantially improved essentially as a result of reducing the magnitude of the SIS residuals near 1 keV present in the fits of the 1T+BREM models. The fits of NGC 1399 and NGC 4472 are further improved when adding a BREM

component (2T+BREM), though the reduction in  $\chi^2$  is not so large as those observed between the 1T+BREM and 2T cases. The fit of the 2T+BREM model of NGC 4472 is formally very acceptable ( $P = 0.42$ ) while those for NGC 1399 and NGC 5044 are formally marginal ( $P \sim 0.01$ ). However, as is clear from Figure 3, these models provide quite satisfactory fits considering their simplicity. The cooling flow models for NGC 1399, NGC 4472, and NGC 5044 behave almost exactly as the two-temperature models except that they have slightly lower quality fits as quantified by  $P$ .

NGC 4636, which has lower emission weighted temperature ( $T \sim 0.7$  keV) than the others, has a qualitatively different behavior than the other galaxies. Not only is the 1T+BREM model indicated to be highly unacceptable, replacing the BREM with another MEKAL component does not improve the fit significantly. However, the 2T+BREM model is a much better fit than 1T+BREM, although it is still not formally acceptable. Similarly, the CF+1T model behaves as a pure CF model and has a larger  $\chi^2$  than the 1T+BREM model. A noticeable improvement in the fit is achieved when adding a BREM component, though again the contribution of the 1T component is negligible; i.e. CF+1T+BREM  $\approx$  CF+BREM. Hence, it is clear that  $P$  is substantially improved for NGC 4636 when a bremsstrahlung component is added to the multitemperature models (as is the case for NGC 1399 and NGC 4472 but to a lesser extent).

When the relative abundances of the elements with respect to Fe are allowed to vary the 1T+BREM models are improved significantly; typically only the relative abundances of the  $\alpha$ -process elements Si, S, Ar, Mg, Ne, and O were varied separately in these fits, though in some cases other elements were varied as well (see below). (Note, consistent with BF, we do not find improvement in the fits when the  $\alpha$ -process elements were tied together and fitted as one parameter.) For NGC 1399, NGC 4472, and NGC 5044 these 1T+BREM models are still poor fits ( $P \ll 1$ ) and have much larger values of  $\chi^2$  than do the multitemperature models with fixed relative abundances. However, for NGC 4636 the 1T+BREM variable abundance model is only marginally unacceptable ( $P \sim 10^{-4}$ ) and provides a better fit than the multitemperature models with fixed relative abundances. Allowing for variable relative abundances in the two temperature models only yields modest reductions in  $\chi^2$  except for NGC 4636 where the change is substantial and results in a reasonably good fit.

The relative abundances with respect to Fe obtained from the fits of the 1T+BREM models for some  $\alpha$ -process elements differ markedly from their solar values. For NGC 1399 and NGC 4472 we find that the key improvements in  $\chi^2$  for these models are the result of reducing the abundances of O, Ne, and Mg such that  $Z_{\text{O,Ne}} \approx 0$  and  $Z_{\text{Mg}} \ll Z_{\text{Fe}}$ . For NGC 5044, the Nickel abundance is the most important. (The next important effect is allowing the oxygen abundance to go to zero analogously to NGC 1399 and NGC 4472.) It is clear that these abundances are primarily the result of the 1T+BREM model trying to minimize the SIS residuals near 1 keV (see Figure 2) since over the *ASCA* energy band these elements have their strongest emission lines (O VIII, Ne X, Mg XI and XII, Ni L shell) in the Fe-L energy region (with the exception of O VII and Ni K shell).

Similar results hold for NGC 4636 except that varying

**Table 3.** Quality of Spectral Fits

		1T+BREM		2T	2T+BREM		CF+1T	CF+1T+BREM
		Fix	Var	Fix	Fix	Var	Fix	Fix
N1399:								
MEKAL	$P$	1.9e-17	1.4e-8	2.7e-6	1.4e-2	3.1e-2	3.6e-9	2.9e-4
	$(\chi^2/\text{dof})$	(651.6/373)	(539.1/368)	(509.3/372)	(431.3/369)	(414.8/363)	(553.2/373)	(473.0/372)
RS	$P$	2.2e-16	9.1e-6	3.8e-14	9.4e-10	2.0e-3	...	...
	$(\chi^2/\text{dof})$	(640.1/373)	(496.0/368)	(613.9/372)	(556.3/369)	(446.4/364)	...	...
N4472:								
MEKAL	$P$	5.3e-16	2.7e-9	5.5e-3	0.44	0.66	5.0e-4	2.8e-2
	$(\chi^2/\text{dof})$	(624.3/364)	(537.9/359)	(435.2/363)	(363.6/360)	(342.5/354)	(459.3/364)	(413.9/361)
RS	$P$	3.4e-6	9.4e-3	6.3e-5	1.2e-3	3.9e-2	...	...
	$(\chi^2/\text{dof})$	(498.3/364)	(424.9/359)	(475.6/363)	(446.9/360)	(404.4/356)	...	...
N4636:								
MEKAL	$P$	1.5e-39	1.3e-4	3.2e-39	5.4e-9	1.0e-2	0.00	5.6e-20
	$(\chi^2/\text{dof})$	(1346/727)	(867.2/720)	(1342/726)	(961.9/723)	(806.9/716)	(1786/727)	(1126/724)
RS	$P$	0.00	1.1e-40	0.00	0.00	2.9e-10	...	...
	$(\chi^2/\text{dof})$	(1826/727)	(1349/721)	(1822/726)	(1586/723)	(977.0/717)	...	...
N5044:								
MEKAL	$P$	2.0e-24	1.3e-8	5.6e-3	7.8e-3	...	1.2e-6	2.1e-5
	$(\chi^2/\text{dof})$	(610.0/293)	(439.6/286)	(357.0/292)	(350.4/289)	...	(420.4/292)	(398.1/289)
RS	$P$	2.5e-9	1.9e-8	1.9e-11	6.1e-11	2.2e-6	...	...
	$(\chi^2/\text{dof})$	(457.3/293)	(438.8/287)	(481.4/292)	(471.6/289)	(405.8/283)	...	...

The  $\chi^2$  null hypothesis probability ( $P$ ), the value of  $\chi^2$ , and the number of degrees of freedom (dof) are listed for each model fitted jointly to the SIS and GIS data with normalizations of each data set free parameters. Models where the relative abundances of the elements with respect to Fe are fixed at their solar values are denoted by “fix” and those that allow variable relative abundances are denoted by “var”. “MEKAL” and “RS” indicate whether the 1T and/or 2T thermal plasma components are computed using the MEKAL or Raymond-Smith models respectively. See text for further explanation of these fits.

the abundances of each of the  $\alpha$ -process elements and Nickel significantly improves  $\chi^2$ . Allowing the Na abundance to be a free parameter gives the largest improvement of any element, with Mg showing the next best improvement. (The energies of the strongest Na lines are at  $\sim 1.1$  keV for the He-like ion and 1.24 keV for the the H-like ion.) The resulting Na abundance, though uncertain, is many times solar; note that NGC 1399 has a small  $\chi^2$  improvement if Na is allowed to be a free parameter and also implies a super-solar Na abundance. (These abundances are discussed in more detail in section 3.3.)

In contrast, as stated above, for NGC 1399, NGC 4472, and NGC 5044 the 2T and 2T+BREM models with relative abundances with respect to Fe fixed at their solar values are superior fits to all of the 1T+BREM models. We do not find significant improvement for these galaxies when the relative abundances are varied, although for NGC 4472 the best-fit O abundance is lower than Fe and for NGC 1399 the best-fit O and Mg abundances are lower than Fe. However, these abundances are consistent with the Fe abundances within their 90% error estimates. The abundances for the two-temperature fits of NGC 4636 behave similarly as for their 1T+BREM models.

### 3.2.2 Comparison to Raymond-Smith

It is necessary to address the extent to which our results depend on the accuracy of the plasma code. This is especially important since the key constraints arise from the SIS

data near 1 keV where emission lines from the Fe L shell, which are not so accurately modeled as are the K shell emission lines, dominate the emission. In particular, can reasonable inaccuracies in the plasma code make a spectrum that is actually 1T+BREM look like a 2T and/or 2T+BREM spectrum?

A simple way to test this is to perform the same fits of the previous section and replace the MEKAL plasma model with that of Raymond-Smith (1977, and updates; hereafter RS). Both the MEKAL and RS plasma codes are identical in their treatment of the ionization balance as given by Arnaud & Raymond (1992) for Fe and Arnaud & Rothenflug (1985) for the the other elements. However, the RS code has many fewer lines than does MEKAL, and, more importantly, it does not incorporate the improved calculations of the Fe L shell lines by Liedahl et al. (1995). Although this is not intended as an exhaustive test of all possible problems with the modeling of the Fe L energy region, comparing the results of fitting MEKAL and RS models does give a fair appraisal of the magnitude of the differences of temperatures and abundances due to significantly different modeling of the Fe L shell emission lines.

In analogy to the MEKAL fits of the previous section, we list the null hypothesis probabilities and  $\chi^2$  values for corresponding models in Table 3. Similarly, the RS fits of 1T+BREM and 2T+BREM models for NGC 1399 are displayed in Figure 4. Inspection of Table 3 reveals that, as would be expected, it is again the SIS data in the Fe L shell

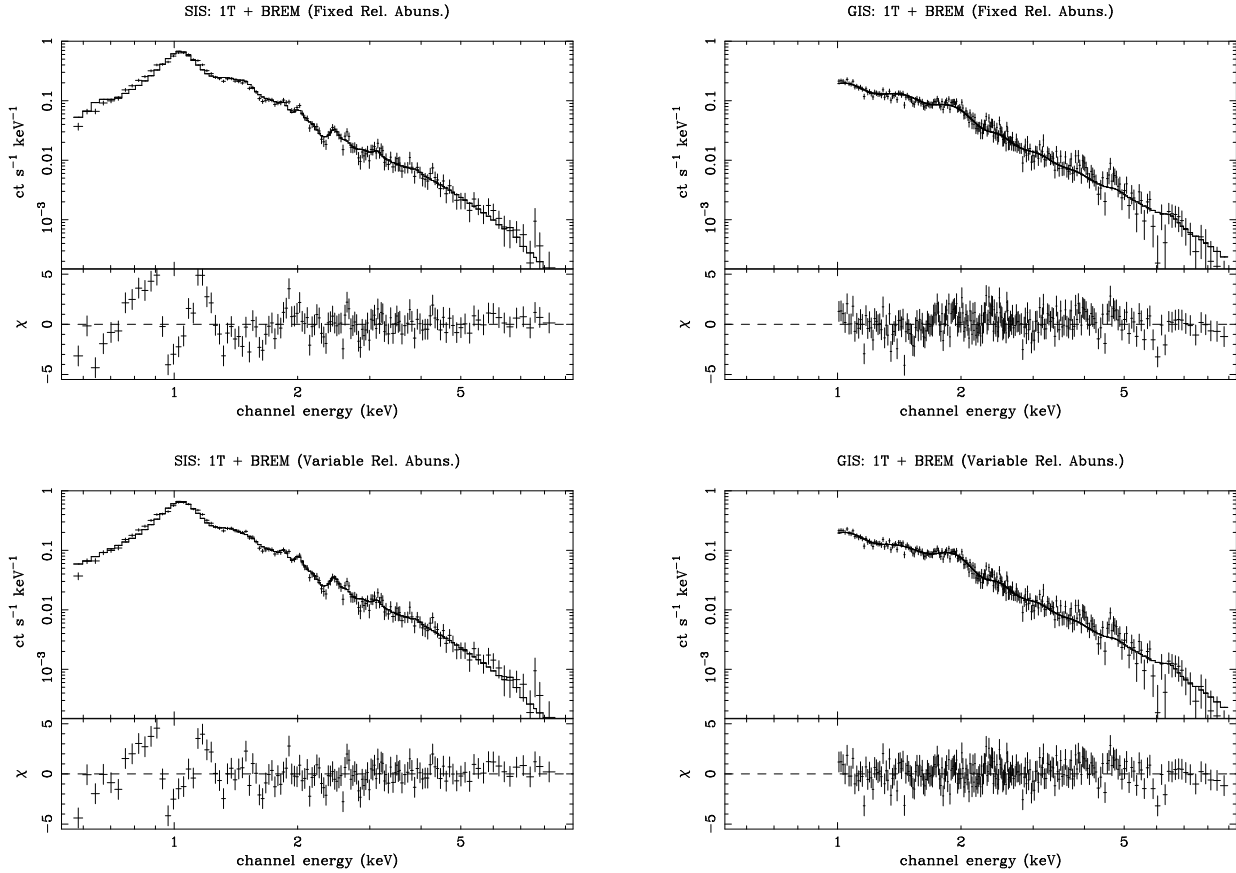


**Figure 2.** Best fitting 1T+BREM models for NGC 1399 for the cases where (1) the relative abundances with respect to Fe are fixed at their solar values (top panels) and (2) the relative abundances are allowed to vary (bottom panels). The models are fit jointly to the SIS and GIS data, but the fits and residuals are shown separately for clarity. The 1T component corresponds to a MEKAL model. See text for further explanation of these models

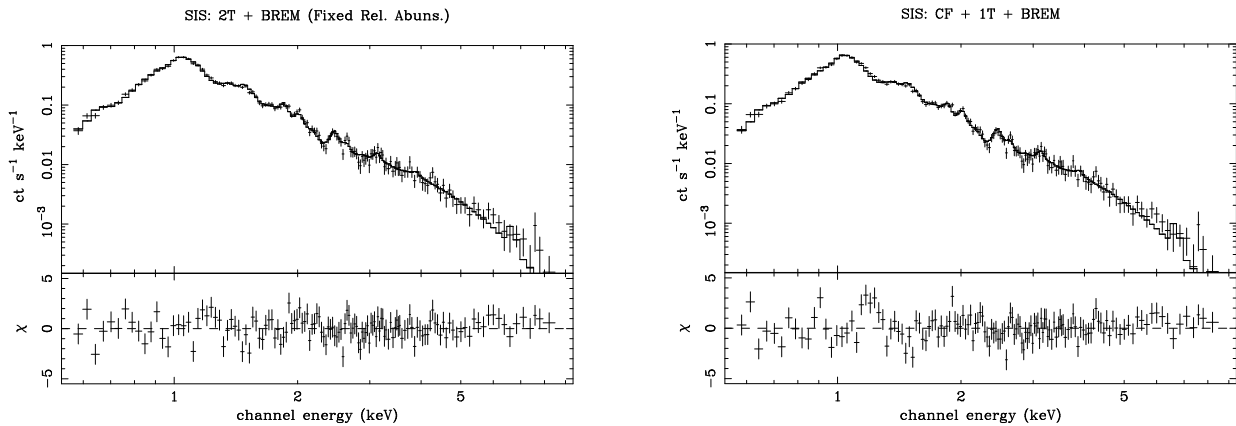


**Figure 3.** As Figure 2 except displayed are the best-fitting 2T+BREM (left) and CF+1T+BREM (right) models. Although each model is fitted jointly to the SIS and GIS data, only the SIS data are shown because the relatively featureless GIS residual patterns are essentially indistinguishable from those in Figure 2.

energy region (see Figure 4) which figure most prominently in the model constraints.

In contrast to the fits with the MEKAL code, the 1T+BREM models with variable relative abundances fit better than two-temperature models that have fixed relative abundances. When allowing for variable relative abundances the two-temperature models do fit better than the

corresponding isothermal models similar to the models with fixed relative abundances. The relative abundances for these two-temperature models are similar to the isothermal models.

Eliminating the Mg abundance is important for both the isothermal and two-temperature RS models. In Figure 4 the prominent absorption feature in the residuals of the

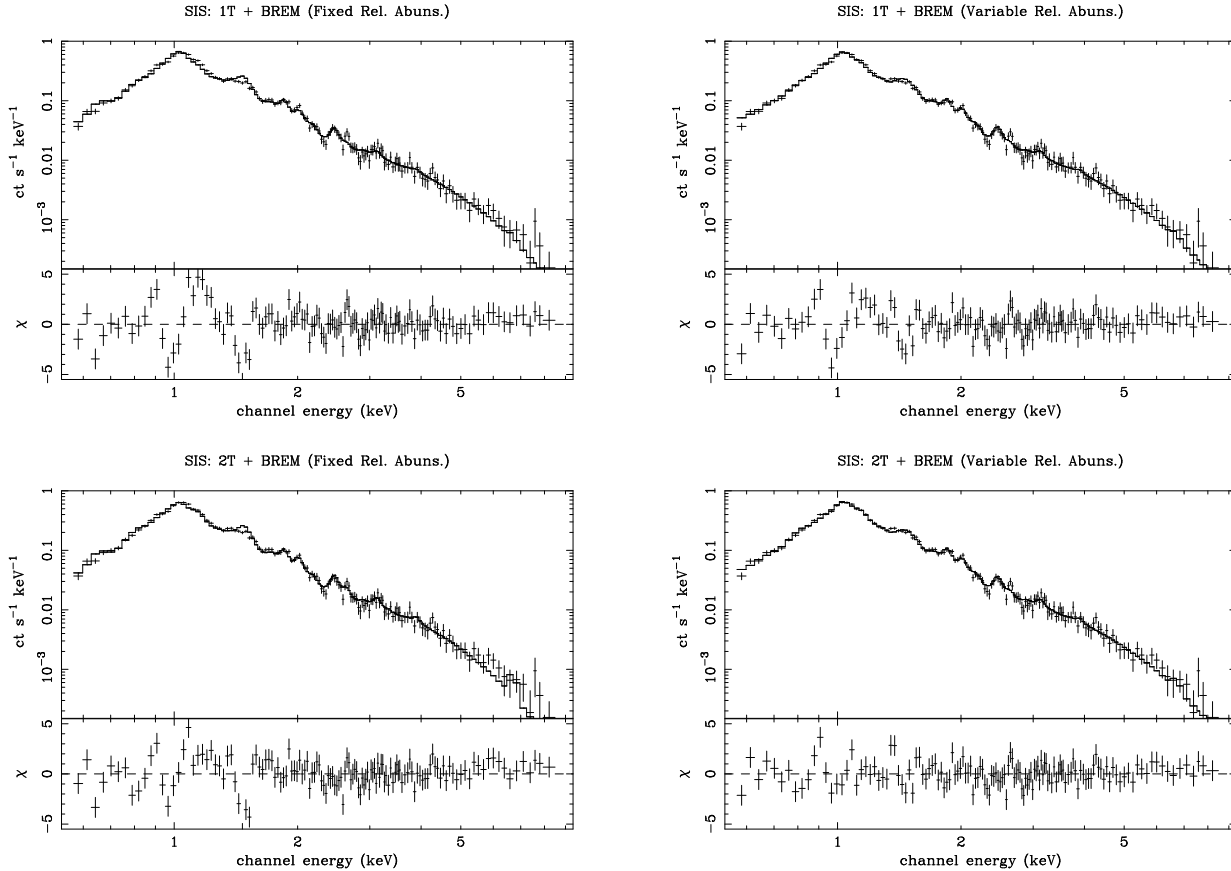


**Figure 4.** As Figure 3 except that Raymond-Smith (RS) code is used for the 1T and 2T model components.

SIS data near 1.5 keV (i.e. near Mg XII  $\text{ly-}\alpha$ ) for the models with fixed relative abundances can be partially compensated for by lowering the Mg abundance to zero. However, as indicated by the residuals of the corresponding variable relative abundance models this procedure does not remove all of the residuals near 1.5 keV.

The best MEKAL model fits (i.e. 2T+BREM) are much better than any fit using RS; this result agrees with the previous study of BF who analyzed the ASCA data of these galaxies using 1T and 2T MEKAL/RS models. Moreover, the relative abundances of several elements with respect to Fe are required to be very different from their solar values for the best 1T+BREM and multitemperature RS fits whereas the multitemperature fits with MEKAL models (except for NGC 4636) provide acceptable fits for the relative abundances fixed at their solar values.

Problems with older plasma codes like RS near 1.5 keV arising from inaccurate 4-2 Fe L transitions were first suggested from analysis of ASCA data of the Centaurus cluster by Fabian et al. (1994). These authors were able to obtain substantially better fits when the energies near 1.5 keV were excluded. Indeed, for NGC 1399 and NGC 4472 which have the highest temperatures in our sample and thus have the most important contribution from the Fe L lines near 1.5 keV, we find significant improvements in the RS fits if we exclude the energies 1.35-1.55 keV. In particular, the two-temperature models with fixed relative abundances now are better fits than all the 1T+BREM models; e.g., for NGC 1399 we obtain ( $\chi^2/\text{dof}/P = 422.2/342/2.0\text{e-}3$ ) for the

1T+BREM variable abundance model and (402.1/341/1.3e-2) for the 2T+BREM fixed relative abundance model. Note, however, that the residuals near 1 keV are still present (as in Figure 4) and thus even when the energies 1.35-1.55 keV are excluded the resulting fits are not as good as with the MEKAL plasma code.

### 3.2.3 Overall assessment

The spectra of the galaxies in our sample generally are better described by models with two thermal plasma components regardless of whether the MEKAL or RS plasma code is employed in the fits; note that it is the SIS data that provide the key constraints. The temperatures derived for the two-temperature MEKAL and RS models are similar and imply multiple phases of hot gas, although the precise values obtained from the MEKAL and RS models differ to some degree as expected (see section 3.3). Given the differences in the modeling of the Fe L shell transitions between these codes, it is evident that such differences are insufficient to cause a spectrum that is actually 1T+BREM to masquerade as a 2T or 2T+BREM system.

The 2T and 2T+BREM models using the MEKAL code with the relative abundances fixed at the solar values are superior fits to all 1T+BREM MEKAL models. Moreover, these two-temperature MEKAL models provide substantially better fits than the 1T+BREM, 2T, and 2T+BREM models which employ the RS code, even when allowing the relative abundances with respect to Fe to vary in the RS

models. The key differences are in the Fe L energy region ( $\sim 0.7 - 1.4$  keV) where the best-fitting two-temperature MEKAL models have negligible residuals (Figure 3) in contrast to the substantial residuals obtained for all best-fit RS models investigated (Figure 4); i.e. the residuals arising from the known errors in the Fe L emission near 1.5 keV of the RS code cannot be removed by adding another temperature component.

Hence, these ASCA data (particularly the SIS) demonstrate that the MEKAL plasma code (as expected) is significantly more accurate than the RS code for the important energies  $\sim 0.7 - 1.4$  keV, and the small residuals for the best-fitting two-temperature MEKAL models imply that remaining inaccuracies in the Fe L energy region for the MEKAL code are insufficient to change qualitatively the results for data of the present quality. Consequently, the results obtained for the models using the MEKAL code should be given precedence over the corresponding results using the RS code.

We thus conclude from the broad-band spectral analysis that (except for possibly NGC 4636) isothermal (1T+BREM) models cannot provide acceptable fits to the ASCA data within the  $r \sim 5'$  apertures of these galaxies.

### 3.3 Detailed properties of models

#### 3.3.1 Calibration and systematic errors

We have examined the reliability of analyzing the summed SIS and summed GIS data for the galaxies in our sample and find that the best-fitting parameters we derived from fitting the summed data sets generally differ by  $< 10\%$  from those derived from simultaneous fitting of the available SIS0, SIS1, GIS2, and GIS3 data sets; usually, the results agree to within a few percent.

For example, consider a 2T MEKAL model (no BREM) fitted to the NGC 1399 SIS data. When fitting the summed SIS data we obtain best-fitting values of  $Z = 1.04Z_{\odot}$  for the metallicity and  $N_{\text{H}}^{\text{c}} = 3.1 \times 10^{21} \text{ cm}^{-2}$  and  $T_{\text{c}} = 0.76$  (keV) for the colder component and  $N_{\text{H}}^{\text{h}} = 0.4 \times 10^{21} \text{ cm}^{-2}$  and  $T_{\text{h}} = 1.72$  (keV) for the hotter component. If instead we simultaneously fit the SIS0 and SIS1 data for the two observation sequences listed in Table 2 (i.e. a total of four data sets) we obtain best-fitting values of  $Z = 1.07Z_{\odot}$  for the metallicity and  $N_{\text{H}}^{\text{c}} = 3.1 \times 10^{21} \text{ cm}^{-2}$  and  $T_{\text{c}} = 0.76$  (keV) for the colder component and  $N_{\text{H}}^{\text{h}} = 0.4 \times 10^{21} \text{ cm}^{-2}$  and  $T_{\text{h}} = 1.72$  (keV) for the hotter component. Hence, the potential inaccuracies involved in combining the individual SIS0/SIS1 and GIS2/GIS3 data appear to be unimportant for the data of the elliptical galaxies in our present study.

We also find this level of agreement with our previous study (BF) which included ASCA data of these galaxies where the simultaneous fitting of the available SIS0 and SIS1 data was emphasized. In BF we tied together the values of  $N_{\text{H}}$  for the colder and hotter components of two-temperature models. However, we have examined the actual data sets that were reduced and analyzed by BF and have obtained results consistent with those stated above when untying the  $N_{\text{H}}$  values. That is, the differences in calibration and data reduction between our study and that of BF do not result in significant differences in the best-fit column densities, temperatures, and abundances.

We do find some evidence for errors in the calibration of the photon energies for the SIS and GIS data. For the galaxies in our sample the fits are generally improved when the redshifts of the SIS and GIS data are allowed to be free parameters. For the example above of the 2T model fitted to the summed SIS and summed GIS data of NGC 1399, the value of  $\chi^2$  is lowered by 35 (372 dof) when the redshifts are allowed to be free parameters. In this case the best-fitting redshift for the SIS is zero and for the GIS  $\sim 0.03$  which implies energy shifts of  $\sim 10$  eV at 2 keV for the SIS and  $\sim 50$  eV for the GIS. (The magnitude of these shifts are not overly sensitive to the model.) These shifts are due to known calibration problems. (See the ASCA GOF WWW pages.) In particular the relatively large shift for the GIS is the result of the energy scale of the GIS RMF being slightly wrong below the Xe-L edge (4.8 keV). (Note that the magnitudes of these shifts are similar if we instead simultaneously fit the SIS0, SIS1, GIS2, and GIS3 data.)

Hence, to account for these (small) calibration errors in the energy scale of the RMFs we always allow the redshifts to be free parameters in our fits; i.e. the model components fitted to the SIS data have one redshift, and those components fitted to the GIS data have a different redshift. Once the best-fitting model is found we freeze the redshifts at their best-fit values for determining error bars on other interesting parameters. This is done to speed up the computations and has no discernible effect on the sizes of the error bars obtained for the other parameters.

For NGC 4636 we find important differences between the SIS0 and SIS1 data at low energies that are not apparent in the data of the other galaxies. In Figure 5 we plot the SIS0 and SIS1 spectral data of NGC 4636 along with the best-fitting 1T+BREM model obtained from joint fitting of the SIS0 and SIS1 data (relative abundances fixed at solar; BREM component modified by Galactic absorption). Above  $\sim 0.8$  keV the residuals of the fit are similar for the SIS0 and SIS1 data as would be expected. However, there is a noticeable discrepancy below  $\sim 0.8$  keV where the residuals of the SIS0 fit lie above those of the SIS1.

These differences at low energies translate to slightly different column densities inferred by the SIS0 and SIS1. If the SIS0 and SIS1 are fitted separately with the 1T+BREM model, we obtain  $N_{\text{H}} = (1.1, 1.5) \times 10^{21} \text{ cm}^{-2}$  for the (SIS0, SIS1) respectively with statistical uncertainties of  $\sim 10\%$  percent. We are unable to affect these low energy differences by changing the event selection criteria of the data. Most importantly, no effect is seen when selecting data with minimal contamination from solar X-rays (i.e. mkf parameter “sunshine=0”).

Differences in  $N_{\text{H}}$  of  $\sim 0.2 \times 10^{21} \text{ cm}^{-2}$  between the SIS0 and SIS1 are expected due to remaining calibration errors in the low energy response of the SIS (see Orr et al. 1998 and the ASCA GOF WWW pages). Although the differences in  $N_{\text{H}}$  for NGC 4636 are about a factor of 2 larger, the discrepancy is reduced to expected levels when the relative abundances are allowed to be free parameters. We have verified that the PV-phase data analyzed by BF also shows these discrepancies, but the effect is of lower significance because of the lower S/N and, presumably, because these calibration errors are smaller for the data taken during the PV-phase (ASCA GOF WWW pages).

However, it should be emphasized that the Fe abun-

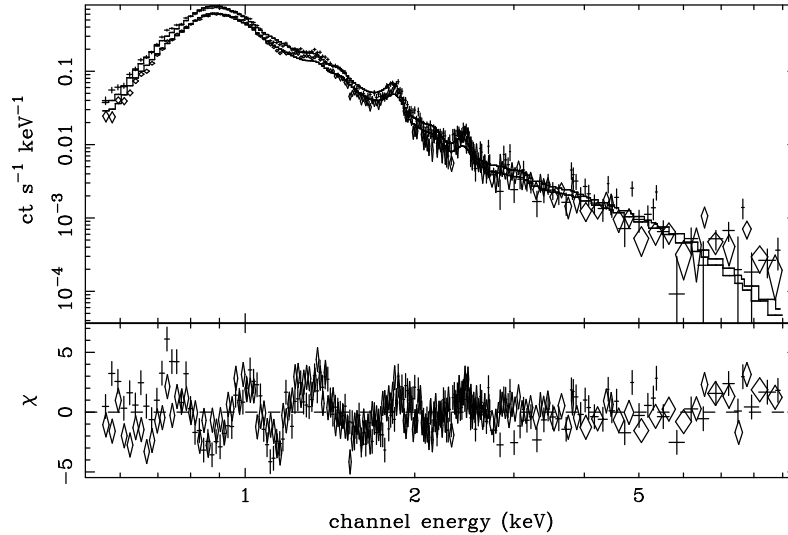


**Figure 5.** The SIS0 (crosses) and SIS1 (diamonds) data of NGC 4636 plotted along with the best-fitting 1T+BREM model (relative abundances with respect to Fe fixed at solar) that is fitted jointly to the two data sets. Note in particular the residuals of the model below  $\sim 0.8$  keV where the SIS0 deviations systematically lie above those of the SIS1 in contrast to the excellent agreement seen at other energies. This is evidence of a relative error in the calibration of the SIS0 and SIS1 response similar to that described for some other sources on the ASCA GOF WWW pages. See text in section 3.3.1 for details.

dance is also affected by these differences in  $N_{\text{H}}$ ; i.e.  $Z_{\text{Fe}} \approx 0.3Z_{\odot}$  for the model fitted to the SIS0 data and  $Z_{\text{Fe}} \approx 0.5Z_{\odot}$  for the SIS1 data. If the relative abundances are varied, this discrepancy for Fe remains but the ratios of other elements to Fe (e.g. Si/Fe) are the same for the SIS0 and SIS1 within statistical errors. The results for these parameters listed below using the summed SIS data thus reflect an average of the results from the SIS0 and SIS1 data.

### 3.3.2 Isothermal models

Recall that our isothermal model (1T+BREM) actually has two components where the first component is an isothermal coronal plasma (MEKAL or RS) modified by variable photo-electric absorption, and the second component is thermal bremsstrahlung modified by absorption fixed at the appropriate Galactic value. We shall focus on the models with variable relative abundances since they provided superior fits for each galaxy (see Table 3 in section 3.2). However, in most cases the results we obtain for the temperatures (plasma and bremsstrahlung), column densities, and Fe abundances of these variable abundance models are quite similar to the case where the relative abundances are fixed at their solar values.

Our procedure for varying the relative abundances with respect to Fe begins with the best-fitting model with relative abundances fixed at the solar values. Then we proceed to untie the abundances of the  $\alpha$ -process elements Si, S, Mg, Ne, and O; a new best-fit model is found after each element is freed. After fitting these parameters we examined whether untying any other elements improved the fits.

In Table 4 we list the best-fitting parameters and 90% confidence limits determined for these 1T+BREM models. We again refer the reader to Figures 2 and 4 for plots of the 1T+BREM models for NGC 1399 and to Figure 6 for

NGC 4636. Related single-temperature fits to the SIS data of NGC 4472 and NGC 5044 are presented in Figure 1 of BF. (The 1T MEKAL models presented in Figure 1 of BF have relative abundances fixed at solar and do not include a BREM component. However, the pattern of residuals is very similar to the 1T+BREM variable relative abundance models.)

The galaxies NGC 1399, NGC 4472, and NGC 5044 have similar spectral properties. Each has  $T \sim 1$  keV for the plasma component and, except for NGC 5044, has a bremsstrahlung temperature at least as high as 6 keV. These high bremsstrahlung temperatures are consistent with emission from discrete sources in these systems (e.g. Canizares et al. 1987; Kim et al. 1992). The hot plasma components dominate these systems with the bremsstrahlung components contributing only  $\sim 0.1\%$  to the total emission measures.

In the case of NGC 5044, the bremsstrahlung temperature is  $T \approx 2$  keV which is inconsistent with emission from discrete sources and rather indicates a contribution from another plasma component in NGC 5044. For the 1T+BREM MEKAL model of NGC 5044 the larger relative contribution ( $\sim 1\%$ ) of this bremsstrahlung component to the total emission measure also supports a plasma origin since NGC 5044, which has a larger  $L_{\text{x}}/L_{\text{B}}$  ratio than the other galaxies, is expected to have a smaller relative contribution to its X-ray emission by discrete sources (e.g. Kim et al. 1992; BF).

Excess absorption above the Galactic value is also indicated for these three galaxies. For NGC 1399 and NGC 4472 the modest excess  $N_{\text{H}}$  implied by the MEKAL model is approximately  $0.2\text{--}0.3 \times 10^{21} \text{ cm}^{-2}$  which is probably significant within the uncertainties in the low energy calibration of the SIS as discussed in section 3.3.1. (The columns inferred using the RS model are within a factor of 2 of these values.) However, for NGC 5044 the inferred (MEKAL)  $N_{\text{H}}$  exceeds the Galactic value by over  $1 \times 10^{21} \text{ cm}^{-2}$ . These values of  $N_{\text{H}}$

**Table 4.** Parameters of Isothermal and Two-Temperature Models

	NGC 1399		NGC 4472		NGC 5044		NGC 4636	
	MEKAL	RS	MEKAL	RS	MEKAL	RS	MEKAL	RS
Isothermal Model								
1T:								
$N_{\text{H}}$ ( $10^{21}$ cm $^{-2}$ )	0.45 $^{+0.13}_{-0.14}$	0.66 $^{+0.19}_{-0.16}$	0.37 $^{+0.17}_{-0.15}$	0.72 $^{+0.28}_{-0.26}$	1.74 $^{+0.46}_{-0.42}$	0.74 $^{+0.22}_{-0.18}$	0.24 $^{+0.19}_{-0.19}$	0.43 $^{+0.13}_{-0.12}$
$T$ (keV)	1.25 $^{+0.02}_{-0.02}$	1.11 $^{+0.01}_{-0.01}$	1.04 $^{+0.02}_{-0.02}$	1.02 $^{+0.02}_{-0.02}$	0.70 $^{+0.02}_{-0.02}$	0.95 $^{+0.02}_{-0.02}$	0.66 $^{+0.01}_{-0.01}$	0.66 $^{+0.01}_{-0.01}$
$EM_{\text{sis}}$	10.37 $^{+0.66}_{-0.75}$	10.41 $^{+0.94}_{-1.54}$	10.56 $^{+1.05}_{-1.01}$	10.29 $^{+0.97}_{-1.47}$	23.79 $^{+9.72}_{-14.16}$	25.48 $^{+3.45}_{-3.06}$	2.93 $^{+1.11}_{-1.18}$	8.88 $^{+0.63}_{-0.60}$
$EM_{\text{gis}}$	15.80 $^{+1.02}_{-1.12}$	15.88 $^{+1.42}_{-2.34}$	15.36 $^{+1.52}_{-1.50}$	15.54 $^{+1.42}_{-2.27}$	33.64 $^{+14.36}_{-20.12}$	38.43 $^{+5.69}_{-5.02}$	3.79 $^{+1.43}_{-1.52}$	11.17 $^{+0.76}_{-0.73}$
Fe	0.35 $^{+0.03}_{-0.03}$	0.43 $^{+0.08}_{-0.05}$	0.28 $^{+0.03}_{-0.03}$	0.41 $^{+0.08}_{-0.05}$	0.22 $^{+0.35}_{-0.07}$	0.31 $^{+0.04}_{-0.03}$	0.80 $^{+0.48}_{-0.21}$	0.16 $^{+0.02}_{-0.02}$
O	0.00 $^{+0.05}_{-0.00}$	0.00 $^{+0.15}_{-0.00}$	0.00 $^{+0.06}_{-0.00}$	0.09 $^{+0.23}_{-0.09}$	0.24 $^{+0.47}_{-0.18}$	0.00 $^{+0.12}_{-0.00}$	0.46 $^{+0.29}_{-0.16}$	0.14 $^{+0.06}_{-0.05}$
Ne	0.00 $^{+0.07}_{-0.00}$	0.03 $^{+0.26}_{-0.03}$	0.00 $^{+0.07}_{-0.00}$	0.00 $^{+0.16}_{-0.00}$	1.18 $^{+1.78}_{-0.36}$	0.00 $^{+0.05}_{-0.00}$	2.16 $^{+1.44}_{-0.62}$	0.00 $^{+0.03}_{-0.00}$
Mg	0.01 $^{+0.13}_{-0.01}$	0.00 $^{+0.02}_{-0.00}$	0.10 $^{+0.10}_{-0.10}$	0.00 $^{+0.10}_{-0.00}$	0.36 $^{+0.61}_{-0.14}$	0.15 $^{+0.07}_{-0.06}$	1.83 $^{+1.28}_{-0.54}$	0.30 $^{+0.04}_{-0.04}$
Si	0.45 $^{+0.08}_{-0.07}$	0.43 $^{+0.08}_{-0.07}$	0.40 $^{+0.07}_{-0.07}$	0.40 $^{+0.09}_{-0.06}$	0.50 $^{+0.72}_{-0.15}$	0.30 $^{+0.07}_{-0.05}$	1.69 $^{+1.13}_{-0.47}$	0.50 $^{+0.05}_{-0.04}$
S	0.40 $^{+0.11}_{-0.10}$	0.44 $^{+0.12}_{-0.11}$	0.48 $^{+0.11}_{-0.12}$	0.49 $^{+0.14}_{-0.12}$	0.65 $^{+0.86}_{-0.22}$	0.28 $^{+0.09}_{-0.08}$	2.42 $^{+0.67}_{-0.32}$	0.83 $^{+0.12}_{-0.11}$
Na	...	...	...	...	...	...	21 $^{+16}_{-7}$	...
Ni	...	...	...	...	3.17 $^{+5.10}_{-1.06}$	0.53 $^{+0.18}_{-0.15}$	0.00 $^{+0.26}_{-0.00}$	1.96 $^{+0.19}_{-0.17}$
BREM:								
$T$ (keV)	> 14	> 6	> 7	> 6	1.93 $^{+0.97}_{-0.49}$	3.58 $^{+3.31}_{-1.28}$	5.22 $^{+2.58}_{-1.29}$	> 17
$EM_{\text{sis}}$	0.11 $^{+0.03}_{-0.03}$	0.12 $^{+0.08}_{-0.03}$	0.07 $^{+0.05}_{-0.03}$	0.08 $^{+0.04}_{-0.04}$	0.59 $^{+0.62}_{-0.30}$	0.07 $^{+0.07}_{-0.04}$	0.07 $^{+0.02}_{-0.01}$	0.08 $^{+0.01}_{-0.01}$
$EM_{\text{gis}}$	0.20 $^{+0.05}_{-0.05}$	0.18 $^{+0.12}_{-0.04}$	0.15 $^{+0.07}_{-0.05}$	0.16 $^{+0.05}_{-0.07}$	1.12 $^{+0.96}_{-0.51}$	0.21 $^{+0.18}_{-0.10}$	0.09 $^{+0.02}_{-0.02}$	0.08 $^{+0.01}_{-0.01}$
Two-Temperature Model								
2T: (colder+hotter)								
$N_{\text{H}}^{\text{c}}$ ( $10^{21}$ cm $^{-2}$ )	4.91 $^{+0.64}_{-0.89}$	5.40 $^{+1.85}_{-4.36}$	2.86 $^{+0.62}_{-0.93}$	5.93 $^{+3.69}_{-1.53}$	2.47 $^{+0.51}_{-0.61}$	7.79 $^{+2.21}_{-2.61}$	0.02 $^{+0.01}_{-0.01}$	0.81 $^{+0.41}_{-0.39}$
$N_{\text{H}}^{\text{h}}$ ( $10^{21}$ cm $^{-2}$ )	0.07 $^{+0.32}_{-0.07}$	0.34 $^{+0.29}_{-0.34}$	0.04 $^{+0.70}_{-0.04}$	0.16 $^{+0.51}_{-0.16}$	0.63 $^{+0.42}_{-0.36}$	0.51 $^{+0.29}_{-0.38}$	0.24 $^{+0.41}_{-0.24}$	4.78 $^{+0.44}_{-0.20}$
$T_{\text{c}}$ (keV)	0.69 $^{+0.03}_{-0.03}$	0.71 $^{+0.27}_{-0.07}$	0.72 $^{+0.03}_{-0.03}$	0.71 $^{+0.25}_{-0.27}$	0.70 $^{+0.02}_{-0.03}$	0.56 $^{+0.12}_{-0.10}$	0.52 $^{+0.05}_{-0.06}$	0.24 $^{+0.01}_{-0.01}$
$T_{\text{h}}$ (keV)	1.54 $^{+0.08}_{-0.07}$	1.27 $^{+0.30}_{-0.06}$	1.39 $^{+0.11}_{-0.09}$	1.06 $^{+0.02}_{-0.03}$	1.23 $^{+0.07}_{-0.06}$	0.97 $^{+0.02}_{-0.02}$	0.76 $^{+0.03}_{-0.03}$	0.71 $^{+0.01}_{-0.01}$
$EM_{\text{sis}}^{\text{c}}$	2.49 $^{+0.82}_{-0.71}$	3.67 $^{+2.97}_{-1.64}$	1.67 $^{+0.77}_{-0.79}$	4.22 $^{+1.60}_{-1.45}$	12.92 $^{+3.08}_{-2.85}$	15.32 $^{+26.37}_{-8.77}$	1.75 $^{+0.37}_{-0.45}$	4.29 $^{+2.60}_{-1.31}$
$EM_{\text{gis}}^{\text{c}}$	2.92 $^{+1.46}_{-1.38}$	5.14 $^{+5.12}_{-4.27}$	3.15 $^{+1.64}_{-1.15}$	4.79 $^{+6.64}_{-1.23}$	10.05 $^{+6.11}_{-8.07}$	11.71 $^{+39.57}_{-11.71}$	0.00 $^{+0.55}_{-0.00}$	5.34 $^{+3.20}_{-1.57}$
$EM_{\text{sis}}^{\text{h}}$	2.32 $^{+0.81}_{-0.70}$	6.65 $^{+1.21}_{-2.09}$	1.30 $^{+1.00}_{-0.69}$	4.79 $^{+0.98}_{-1.69}$	9.63 $^{+1.88}_{-1.62}$	19.22 $^{+4.25}_{-6.70}$	2.37 $^{+0.60}_{-0.55}$	4.33 $^{+1.22}_{-1.03}$
$EM_{\text{gis}}^{\text{h}}$	4.39 $^{+1.63}_{-1.40}$	10.78 $^{+2.32}_{-3.33}$	1.54 $^{+1.23}_{-0.72}$	6.92 $^{+1.69}_{-2.62}$	21.56 $^{+8.73}_{-4.45}$	30.67 $^{+8.73}_{-11.04}$	4.69 $^{+1.33}_{-1.29}$	5.81 $^{+1.61}_{-1.29}$
Fe	1.62 $^{+0.74}_{-0.61}$	0.61 $^{+0.25}_{-0.10}$	2.00 $^{+2.40}_{-0.97}$	0.61 $^{+0.30}_{-0.13}$	0.57 $^{+0.10}_{-0.08}$	0.41 $^{+0.18}_{-0.06}$	0.73 $^{+0.28}_{-0.16}$	0.99 $^{+0.45}_{-0.29}$
O	...	0.10 $^{+0.37}_{-0.10}$	...	0.25 $^{+0.47}_{-0.25}$	...	0.11 $^{+0.20}_{-0.11}$	0.39 $^{+0.23}_{-0.14}$	0.14 $^{+0.04}_{-0.05}$
Ne	...	0.76 $^{+0.53}_{-0.44}$	...	0.28 $^{+0.44}_{-0.26}$	...	0.00 $^{+0.15}_{-0.00}$	0.92 $^{+0.26}_{-0.28}$	2.42 $^{+1.11}_{-0.74}$
Mg	...	0.00 $^{+0.16}_{-0.00}$	...	0.18 $^{+0.19}_{-0.11}$	...	0.21 $^{+0.14}_{-0.07}$	1.40 $^{+0.57}_{-0.35}$	1.25 $^{+0.51}_{-0.36}$
Si	...	0.55 $^{+0.13}_{-0.11}$	...	0.52 $^{+0.21}_{-0.12}$	...	0.36 $^{+0.10}_{-0.07}$	1.24 $^{+0.46}_{-0.29}$	1.20 $^{+0.40}_{-0.30}$
S	...	0.55 $^{+0.18}_{-0.13}$	...	0.68 $^{+0.29}_{-0.18}$	...	0.36 $^{+0.11}_{-0.10}$	1.64 $^{+0.46}_{-0.36}$	1.46 $^{+0.40}_{-0.19}$
Na	...	...	...	...	...	...	15 $^{+5}_{-4}$	...
Ni	...	...	...	...	...	0.83 $^{+0.34}_{-0.24}$	0.00 $^{+0.15}_{-0.00}$	4.92 $^{+0.99}_{-1.30}$
BREM:								
$T$ (keV)	5(> 3)	> 5	3.23 $^{+1.35}_{-0.77}$	5.46 $^{+3.21}_{-1.75}$	...	2.65 $^{+1.29}_{-0.70}$	9 > 5	> 12
$EM_{\text{sis}}$	0.16 $^{+0.23}_{-0.07}$	0.10 $^{+0.08}_{-0.03}$	0.18 $^{+0.06}_{-0.05}$	1.59 $^{+0.33}_{-0.56}$	...	0.15 $^{+0.11}_{-0.07}$	0.06 $^{+0.02}_{-0.01}$	0.05 $^{+0.03}_{-0.01}$
$EM_{\text{gis}}$	0.21 $^{+0.32}_{-0.11}$	0.16 $^{+0.12}_{-0.04}$	0.32 $^{+0.16}_{-0.15}$	2.29 $^{+0.56}_{-0.87}$	...	0.38 $^{+0.24}_{-0.16}$	0.06 $^{+0.02}_{-0.01}$	0.05 $^{+0.03}_{-0.01}$

Best-fitting values and 90% confidence limits on one interesting parameter ( $\Delta\chi^2 = 2.71$ ) are listed for selected isothermal and two-temperature models jointly fit to the SIS and GIS data. We list results for each model using both the MEKAL and Raymond-Smith (RS) plasma codes. (See Table 3 for the  $\chi^2$  values of these models.) The isothermal models are 1T+BREM models with variable relative abundances. Only the abundances listed with error estimates are free parameters; the remaining abundances (not listed) and those with “...” are tied to Fe. All abundances are quoted in units of their (photospheric) solar values (Anders & Grevesse 1989). The emission measures ( $EM$ ) are quoted in units of  $10^{-17} n_e n_p V / 4\pi D^2$  similar to what is done in XSPEC. (We have converted the BREM emission measures to this standard as well.) The BREM component is also modified by photo-electric absorption fixed at the Galactic value (see Table 1). For the two-temperature models the abundances for the colder and hotter temperature components are tied together in the fits.

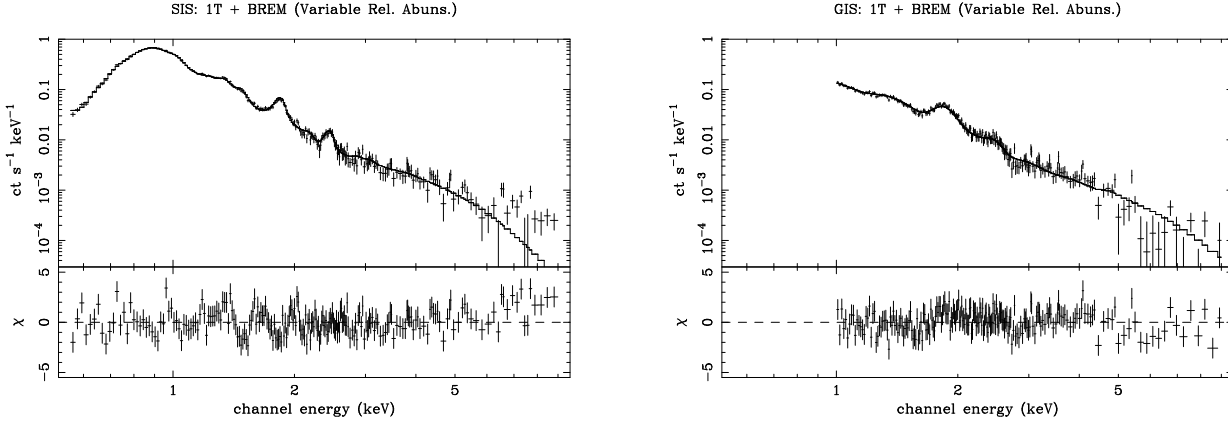


**Figure 6.** Best-fitting 1T+BREM (MEKAL) model with variable relative abundances for NGC 4636. The models are fitted jointly to the SIS and GIS data, and for display purposes only the energy bins above  $\sim 5$  keV have been re-binned such that  $S/N > 3$  in each bin. The parameters of these plots are listed in Tables 4 and 5.

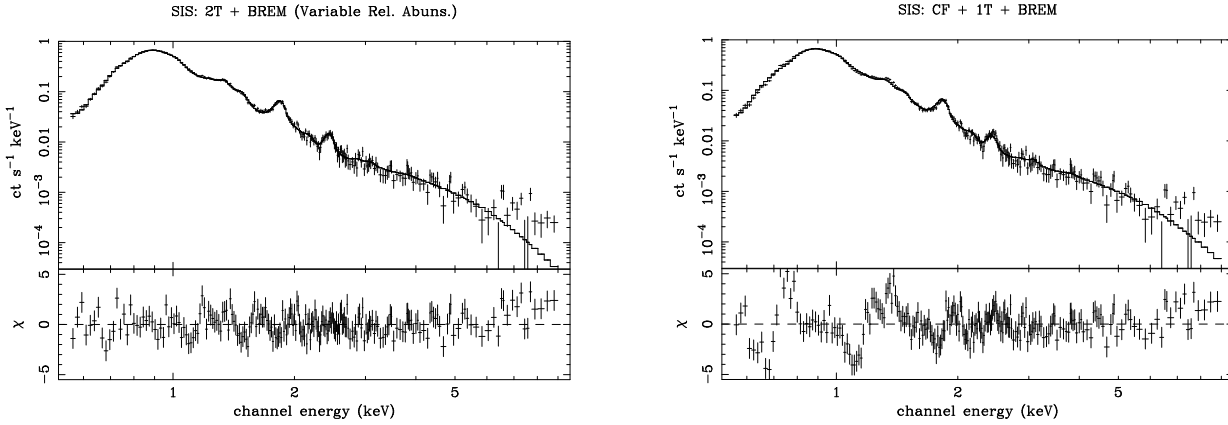


**Figure 7.** As Figure 6 except the 2T+BREM and CF+1T+BREM models are displayed. Although these models were fitted jointly to the SIS and GIS data, only the SIS data are shown.

depend on the model, but excess absorption in the brightest ellipticals appears to be common (BF).

These results for the temperatures and column densities generally agree with previous studies that have fit similar 1T and/or 1T+BREM models to the SIS and GIS data of these galaxies (or 2T models to only the GIS data); e.g. Awaki et al. 1994; Matsushita et al. 1994; Fukazawa et al. 1996; Arimoto et al. 1997; Matsumoto et al. 1997; BF. Similar agreement is found for the Fe abundances. We find that  $Z_{\text{Fe}} \sim 0.3 (< 0.5) Z_{\odot}$  for NGC 1399, NGC 4472, and NGC 5044 for these models, and we again remark that these values are essentially unchanged for models where the relative abundances of the elements are fixed at their solar values.

The Si and S abundances are consistent with Fe for NGC 1399 and the RS models of NGC 4472 and NGC 5044, but they exceed Fe for the MEKAL models of NGC 4472 and NGC 5044. The Si and S abundances obtained for the RS models are consistent with previous published results for NGC 4472 (Awaki et al. 1994) and NGC 5044 (Fukazawa et al. 1996) considering the small differences in calibration, extraction regions, and background between those studies and ours.

In contrast to previous studies, we find that varying each of the O, Ne, and Mg abundances has an important

contribution to lowering  $\chi^2$  and each abundance is, for the most part, very different from Fe. The O, Ne, and Mg abundances are approximately zero for NGC 1399 and NGC 4472. This situation is similar for NGC 5044 for the RS case, but when the plasma component is a MEKAL model the O and Mg abundances are essentially consistent with the Fe abundance. The Ne abundance, however, is about 6 times larger than Fe.

Because these models are poor fits to the SIS data around 1 keV for NGC 1399, NGC 4472, and NGC 5044, these abundances unlikely have physical meaning. However, as we discussed in section 3.2 errors in the plasma codes are not the key reason for the poor fits. We can illustrate this further by considering the Mg abundance.

As we mentioned at the end of section 3.2.2, a serious error in the RS (and old MEKA) plasma code near the strong Mg transitions ( $\sim 1.5$  keV) was noted first by Fabian et al. (1994). The MEKAL code includes new computations of the 4-2 transitions of Fe to correct these errors. However, we find that the Mg abundance is zero for both the RS and MEKAL isothermal models of NGC 1399 and NGC 4472. If indeed a zero Mg abundance is unphysical, then a different model for the temperature structure is probably required rather than more precise atomic physics calculations.

For NGC 5044 the situation is complicated because we find that the fits are substantially improved when Ni is allowed to be a free parameter for the MEKAL case though only modestly improved for RS. Although the implied large Ni abundance ( $Z_{\text{Ni}} \approx 3Z_{\odot}$ ) could indicate other inaccuracies in the MEKAL plasma code, the  $\sim 2$  keV bremsstrahlung temperature already shows that a model of an isothermal plasma with discrete sources is inadequate. Thus, like NGC 1399 and NGC 4472, the abundances and temperatures for NGC 5044 themselves show the inadequacy of the 1T+BREM model as already indicated by the poor quality of the fits described in section 3.2.

NGC 4636 has a lower plasma temperature ( $\approx 0.66$  keV) than the other galaxies in our sample which is similar for both the MEKAL and RS models. However, of all the galaxies in our sample NGC 4636 shows the most dramatic difference in the quality of the fits between models using the MEKAL code and those using the RS code (see Table 3). For the 1T+BREM model with variable relative abundances we obtained a decent fit ( $P \sim 10^{-4}$ ) using the MEKAL code whereas a totally unacceptable fit ( $P \sim 10^{-40}$ ) was obtained for the RS code. Residuals are still prominent for the MEKAL case in both the SIS and GIS data (see Figure 6), and we shall consider these below.

The inferred column densities for the 1T+BREM model of NGC 4636 imply a slight excess above the Galactic value that is consistent with the Galactic value within the errors in the low-energy calibration of the SIS. The  $\sim 5$  keV bremsstrahlung temperature of the MEKAL model can be reasonably attributed to discrete sources (as is the case for the 1T+BREM RS model). These results for the temperatures of the plasma and bremsstrahlung components and for the column densities are not substantially different if the relative abundances are fixed at their solar values in the fits; e.g. plasma temperatures increase to  $\sim 0.75$  keV – see section 4.

The abundances differ substantially for the MEKAL and RS 1T+BREM models of NGC 4636. The abundances of most of the elements determined using the MEKAL model greatly exceed those determined using RS. The Fe abundance is  $\approx 0.8$  solar for the MEKAL model versus  $\approx 0.2$  solar for the RS model. (Note that the MEKAL Fe abundance is lowered to  $\approx 0.6$  solar if the relative abundances are fixed at their solar values.) However, the relative abundances of Mg, Si, and S are not too dissimilar for the MEKAL and RS models; i.e. Mg/Fe, Si/Fe  $\sim 2$  and S/Fe  $\sim 3$  for MEKAL while Mg/Fe  $\sim 2$ , Si/Fe  $\sim 3$  and S/Fe  $\sim 5$  for RS. The O abundance is consistent with the Fe abundance for RS but is about half that of Fe for MEKAL.

In contrast, the Ne, Na, and Ni abundances have striking qualitative differences for the MEKAL and RS 1T+BREM models for NGC 4636. First, Ne is zero for RS while about twice solar for MEKAL. Second, the fits of both models are significantly improved when allowing the Ni abundance to be a free parameter, but the resulting value is very different in both cases: zero Ni abundance for MEKAL and  $\sim 2Z_{\odot}$  for RS. Finally, the MEKAL fit is also substantially improved if the Na abundance is allowed to be a free parameter with a best fit value of  $\sim 21Z_{\odot}$ ; RS does not have any Na lines in its code.

Our results for NGC 4636 are not inconsistent with those of Matsushita et al. (1997) who analyzed the same

deep ASCA observation. These authors fit 1T+BREM models jointly to the SIS and GIS data where: (1) the bremsstrahlung temperature was fixed at 10 keV; (2) the abundances of Fe and Ni were tied together and fitted as a free parameter; (3) the abundances of O, Ne, Mg, Si, and S (and the rest of the elements) were tied together and fitted as one free parameter. They were unable to obtain an acceptable fit with any plasma model (e.g. MEKAL and RS) to the Fe L energy region using this method. This is consistent with our results since we required separate fitting of several of the abundances they tied together to obtain an acceptable fit.

Matsushita et al.’s solution was instead to add a systematic error to the data in the Fe L region. (This is tantamount to excluding the Fe L data – a procedure we do not favor because (1) the Fe L lines are the most important for constraining the temperatures and Fe abundances of ellipticals, and (2) we are able to obtain good fits for the other galaxies with the Fe L included.) Upon excluding the Fe L region they obtained acceptable fits for the MEKAL model (and other models) with Fe and Ni abundances of  $\sim 0.9Z_{\odot}$  and an abundance of  $\sim 1.1Z_{\odot}$  for the rest. These abundances (aside from Ni) are consistent with our results in Table 4 if the  $\alpha$ -process abundances are tied together in the fits. The principal difference between our results and those of Matsushita et al. is that we have narrowed down the locations of candidate problematic emission lines in the Fe L regions: i.e. energies near the strongest O, Na, and Ni lines. Below in section 3.3.5 we discuss the implications of these abundances for the plasma codes.

### 3.3.3 Two-temperature models

Next we consider the two-temperature models consisting of two thermal plasma components (each modified by their own photo-electric absorption) with or without a thermal bremsstrahlung component (modified by Galactic absorption) to account for emission from discrete sources. The abundances of the two plasma components are tied together as we did not obtain significant improvement in the fits when doing otherwise. We initially determined the best-fitting 2T or 2T+BREM models with the relative abundances fixed at their solar values; for the 2T+BREM case the BREM component is added after the best 2T model is obtained. Then, analogously to the isothermal models, the abundances of the  $\alpha$ -process elements (and others) are untied sequentially until the best fit was achieved.

Recall from section 3.2 (Table 3) that the 2T MEKAL models with relative abundances fixed at their solar values are substantially better fits than isothermal (1T+BREM) models for NGC 1399, NGC 4472, and NGC 5044. The temperatures for the “colder” components are typically  $T_c \sim 0.7$  keV and for the “hotter” components  $T_h \sim 1.2$ -1.6 keV for the MEKAL models. These values indicate different temperatures in the hot gas and are inconsistent with the temperatures expected for discrete sources in agreement with the results of BF for these galaxies.

If a bremsstrahlung component is added to these galaxies there is some small improvement in the fits for NGC 1399 and NGC 4472 though essentially no improvement for NGC 5044 (Table 3). We list the 2T+BREM model parameters for NGC 1399 and NGC 4472 in Table 4. For NGC 5044

we list the 2T model parameters for the MEKAL plasma code because the bremsstrahlung component is not clearly required by the fits; however, for illustration, we do give the 2T+BREM parameters for the RS code.

The values of  $T_c$  are mostly unaffected by the addition of the bremsstrahlung component, though the values of  $T_h$  decrease by  $\sim 0.2$  keV for NGC 1399 and NGC 4472. For NGC 1399 the temperature of the bremsstrahlung component is consistent with discrete sources, but the  $\sim 3$  keV temperature (MEKAL) for NGC 4472 is perhaps too low and may indicate additional temperature structure in the hot gas.

The column densities for the colder and hotter components of NGC 1399, NGC 4472, and NGC 5044 are very similar. Excess absorption above the Galactic value is strongly indicated for the colder components in these galaxies with  $N_H$  ranging from about  $2\text{--}5 \times 10^{21}$  cm $^{-2}$ . In contrast, the absorption of the hotter components is small and consistent with the Galactic value for each of these galaxies.

This distinction in column densities between the colder and hotter components for elliptical galaxies has not been reported previously. (In BF we tied together the columns of the colder and hotter components, though upon re-examining the data analyzed by BF we have verified the differences between the two components for these galaxies.) This pattern of excess intrinsic absorption on the colder gas which is presumably more centrally concentrated than the hotter gas (having only Galactic absorption) is similar to what is found in the cores of some galaxy clusters with strong cooling flows (e.g. Fabian 1994).

The emission measures of the colder and hotter components of NGC 1399, NGC 4472, and NGC 5044 are approximately equal such that  $0.5 \lesssim EM^c/EM^h \lesssim 1$ . Although for NGC 1399 and NGC 5044  $EM^c/EM^h$  is larger for the SIS as would be expected because it is more sensitive to energies  $\sim 0.5\text{--}1$  keV, this is not the case for NGC 4472. That is, there is no systematic difference in  $EM^c/EM^h$  between the SIS and GIS for these galaxies.

Probably the most significant differences between the parameters of the isothermal and two-temperature models are the Fe abundances for the MEKAL plasma models of NGC 1399, NGC 4472, and NGC 5044. The Fe abundances are approximately 1.6 solar and 2 solar for the 2T+BREM MEKAL models for NGC 1399 and NGC 4472 compared to approximately 0.3 solar for the isothermal models. For the 2T models the Fe abundances of NGC 1399 and NGC 4472 are  $\sim 1.1$  solar and have smaller error bars in excellent agreement with the results in Table 5 of BF. That is, adding the bremsstrahlung component significantly loosens the constraints on the upper limit of the Fe abundance for the two-temperature MEKAL model. When determining the upper limits for the Fe abundances obtained from the 2T+BREM models, the bremsstrahlung temperatures were fixed to the best-fit values; i.e. for NGC 1399 and NGC 4472.

The Fe abundance for the 2T MEKAL model for NGC 5044 ( $\sim 0.6$  solar) is also larger than that determined from the isothermal model ( $\sim 0.2$  solar) also in good agreement with Table 5 of BF. These large differences in the Fe abundances between the isothermal and two-temperature models highlight the importance of finding the correct emission measure distribution as a function of temperature for interpreting the abundances derived from spectral fitting, a point

that has been stressed in some previous X-ray studies of ellipticals (Buote & Canizares 1994; Trinchieri et al. 1994; BF) and by a recent study of poor galaxy groups (Buote 1999).

As already mentioned in section 3.2, allowing the relative abundances to be free parameters offers no significant improvements in the fits of 2T or 2T+BREM models to NGC 1399, NGC 4472, and NGC 5044 using the MEKAL plasma code. In contrast, the abundances of the two-temperature RS models behave very similarly to their isothermal counterparts except that the error bars are larger for the two-temperature case as would be expected. (Note if the energies 1.35 - 1.55 keV are excluded from the RS fits to NGC 1399 and NGC 4472, the 2T+BREM models with fixed relative abundances have larger Fe abundances:  $\sim 1.0Z_\odot$  for NGC 1399 and  $\sim 0.8Z_\odot$  for NGC 4472; cf. end of section 3.2.2.)

For NGC 4636 the 2T+BREM MEKAL model with variable relative abundances offers some improvement over the variable abundance 1T+BREM model as discussed in section 3.2. Only the SIS data actually require the additional temperature component (Table 4):  $T_c \sim 0.5$  keV and  $T_h \sim 0.75$  keV. The absorbing columns on both components are consistent with zero and the abundances are very similar to those obtained for the 1T+BREM case.

Although the 2T+BREM and 1T+BREM models with variable relative abundances give marginally acceptable fits to the data in terms of  $\chi^2$  it is clear from the residuals of the fits (Figure 7) that the energies below 2 keV are still not adequately modeled. Moreover, the highly significant super-solar Na abundance and zero Ni abundance for these models places added doubt on the correctness of these models for NGC 4636.

The 2T+BREM RS model, in contrast, offers a substantial improvement in the fit over the 1T+BREM models for NGC 4636, though the fit is still not as good as that with the MEKAL model. The temperature of the colder component,  $T_c \sim 0.25$  keV, is half that derived for the MEKAL model. Moreover, substantial excess absorption is required for the hotter component (larger than that for the colder component) unlike for the MEKAL model for NGC 4636 and the other galaxies in the sample. The Fe abundance for the 2T+BREM RS model is about 1 solar, more than five times the value obtained for the 1T+BREM models. Although most of the other abundances are also larger for the 2T+BREM case, the O abundance remains small (0.14 solar) while the Ni abundance is even larger than before (about 4 solar). Again, like the case of the MEKAL model the 2T+BREM RS model has significant residuals below 2 keV and abundances (especially Ni) that cast doubt on the model.

Finally, we have computed the 0.5-10 keV luminosities of the BREM components for the 2T+BREM models of NGC 1399, NGC 4472, and NGC 4636. Using the values of  $L_B$  listed in Table 1 of BF we obtain best-fitting results for  $L_x/L_B$  of 0.006 for NGC 1399, 0.001 for NGC 4472, and 0.002 for NGC 4636. These ratios are consistent within their 90% errors indicating that the BREM components are consistent with the expectation that the X-ray emission from discrete sources should be proportional to  $L_B$ .

**Table 5.** Parameters of Cooling Flow Models

	NGC 1399	NGC 4472	NGC 5044	NGC 4636
CF:				
$N_{\text{H}}$ ( $10^{21}$ cm $^{-2}$ )	$2.96^{+0.27}_{-0.26}$	$2.86^{+0.29}_{-0.26}$	$3.20^{+0.27}_{-0.26}$	$1.44^{+0.25}_{-0.24}$
$T$ (keV)	$1.62^{+0.10}_{-0.08}$	$1.30^{+0.11}_{-0.06}$	$1.15^{+0.07}_{-0.05}$	$0.73^{+0.01}_{-0.01}$
$Z(Z_{\odot})$	$1.14^{+0.43}_{-0.22}$	$1.41^{+0.59}_{-0.43}$	$0.79^{+0.88}_{-0.22}$	$1.04^{+0.35}_{-0.18}$
$\dot{M}_{\text{sis}}$ ( $M_{\odot}$ yr $^{-1}$ )	$1.62^{+0.20}_{-0.18}$	$2.54^{+0.34}_{-0.37}$	$41.32^{+4.59}_{-5.42}$	$2.65^{+0.45}_{-0.40}$
$\dot{M}_{\text{gis}}$ ( $M_{\odot}$ yr $^{-1}$ )	$3.90^{+0.61}_{-0.67}$	$4.56^{+0.81}_{-0.96}$	$27.09^{+20.80}_{-23.76}$	$1.03^{+1.34}_{-0.93}$
1T:				
$N_{\text{H}}$ ( $10^{21}$ cm $^{-2}$ )	$0.02^{+0.01}_{-0.01}$	$0.00^{+0.88}_{-0.00}$	$0.67^{+0.65}_{-0.64}$	$2.72^{+0.29}_{-0.29}$
$Z(Z_{\odot})$	...	...	$0.44^{+0.19}_{-0.15}$	...
$EM_{\text{sis}}$	$2.20^{+0.59}_{-0.65}$	$0.85^{+0.55}_{-0.45}$	$6.33^{+2.97}_{-2.55}$	$3.25^{+0.61}_{-0.76}$
$EM_{\text{gis}}$	$0.00^{+1.49}_{-0.00}$	$0.00^{+0.42}_{-0.00}$	$21.25^{+8.53}_{-8.23}$	$5.88^{+1.23}_{-1.41}$
BREM:				
$T$ (keV)	> 4	$3.71^{+6.44}_{-0.98}$	...	> 8
$EM_{\text{sis}}$	$0.06^{+0.07}_{-0.03}$	$0.14^{+0.06}_{-0.08}$	...	$0.06^{+0.03}_{-0.01}$
$EM_{\text{gis}}$	$0.16^{+0.11}_{-0.04}$	$0.28^{+0.11}_{-0.12}$	...	$0.05^{+0.03}_{-0.01}$

Best-fitting and 90% confidence limits on one interesting parameter ( $\Delta\chi^2 = 2.71$ ) are listed for selected cooling flow models;  $\chi^2$  values for these models are listed in Table 3. The temperatures and abundances of the CF and 1T components are tied together in the fits except for the abundances for NGC 5044; the relative abundances with respect to Fe for all the cooling flow models are fixed at solar. The mass deposition rates assume distances of 18 Mpc for NGC 1399, NGC 4472, and NGC 4636 and 39 Mpc for NGC 5044 ( $H_0 = 70$  km s $^{-1}$  Mpc $^{-1}$ ). The bremsstrahlung component is modified by Galactic absorption (Table 1) and the emission measures are quoted in units as explained in Table 4.

### 3.3.4 Multiphase cooling flows

We have learned in section 3.2 that for NGC 1399, NGC 4472, and NGC 5044 the multiphase cooling flows have  $\chi^2$  values approximately midway between those of the 1T+BREM variable relative abundance models and the 2T+BREM models having relative abundances with respect to Fe fixed at their solar values. If only models with solar relative abundances are compared (as is appropriate for the cooling flow models since they are restricted to solar relative abundances) then the cooling flow models have  $\chi^2$  values that are substantially smaller than the 1T+BREM models and similar (though slightly worse) than the 2T+BREM models. For NGC 4636 this also applies if the comparison is restricted to models with solar relative abundances.

The fits of the cooling flow models are quite similar to the two-temperature models of NGC 1399, NGC 4472, and NGC 5044. The pattern of residuals in the SIS data seen for the CF+1T+BREM model for NGC 1399 in Figure 3 are very similar to those of NGC 4472 and to a lesser extent those of NGC 5044. For NGC 4636 (Figure 7) the residuals are larger and more complex.

The properties of the cooling flow models are similar in many important respects to the two-temperature models. In Table 5 we list the derived parameters for CF+1T+BREM models of NGC 1399, NGC 4472, and NGC 4636 and for the CF+1T model of NGC 5044. (The CF+1T model is focused on for NGC 5044 since a bremsstrahlung component is not required as also found for the isothermal and two-temperature models.) The temperatures of the isothermal components (which also equal the maximum temperature of the cooling flow components) are very similar to  $T_{\text{h}}$  for the two-temperature models (Table 4). The emission-weighted

temperatures of the cooling flow components are also approximately equal to  $T_{\text{c}}$  (using  $\langle T \rangle \approx 0.6T - \text{Buote et al. 1998}$ ).

Moreover for NGC 1399, NGC 4472, and NGC 5044, analogously to the two-temperature models, the ‘‘hotter’’ component of the cooling flow models (i.e. 1T component) has small absorption consistent with zero whereas the colder component (i.e. CF component) requires significant absorption in excess of the Galactic value. Excess absorption somewhat larger than the cooling-flow component is indicated for the 1T component of NGC 4636 similar to the two-temperature MEKAL model.

The metal abundances for the cooling flows are also reasonably consistent with the two-temperature models. For NGC 5044 we are able to place interesting constraints on the metal abundances of both the cooling flow and isothermal components. We find that the abundance of the cooling flow is about 0.8 solar which is twice that of the isothermal component. The principal reason for this constraint is the lack of an additional bremsstrahlung component; i.e. adding a bremsstrahlung component weakens this constraint, but the best-fit abundances still indicate a higher abundance for the cooling flow component. This also applies to NGC 1399 and NGC 4472: if the bremsstrahlung component is omitted, the abundance of the cooling flow component tends to exceed the isothermal component, though at a lower significance level than found for NGC 5044.

The mass deposition rates of a few solar masses per year are typical for ellipticals (e.g. BF). However, the large  $\dot{M}_{\text{sis}} \sim 40 M_{\odot}$  yr $^{-1}$  for NGC 5044 is even larger than for typical galaxy groups (Buote 1999) and is in fact more similar to that of a galaxy cluster (e.g. Fabian 1994).

### 3.3.5 Remaining problems with Fe L in the plasma codes

Although, as we discussed in section 3.2.3, the MEKAL code is superior to the RS code for analysis of ASCA data of the elliptical galaxies in our sample, it is likely that problems still exist in the MEKAL code. Examination of the (admittedly small) SIS residuals for the two-temperature fits of NGC 1399 (Figure 3) reveals systematic excesses near 1.1 keV and 0.9 keV (and elsewhere to a lesser extent). Comparing these residuals to those of the cooling flow model for NGC 1399 shows that the residuals at 0.9 keV and 1.1 keV exist for the cooling flow model but are more pronounced. Related behavior is observed for NGC 4472 and NGC 5044. Taken by themselves these small residual patterns reasonably could be attributed to the model of the emission measure distribution as a function of temperature (i.e. 2T+BREM, CF+1T+BREM, etc.) rather than the plasma code.

The case of NGC 4636 lends support to the plasma code explanation. In order to obtain formally acceptable fits to the SIS data of NGC 4636 we require that the Na abundance be 15-20 solar and the Ni abundance be zero: both of these values greatly differ from the derived Fe abundance of 0.8 solar. These abundances of Na and Ni are inconsistent with standard models for the enrichment of the hot gas in ellipticals (e.g. David et al. 1991; Ciotti et al. 1991).

If indeed the super-solar Na abundance is unphysical, then an error in the MEKAL code near 1.1 keV is implied since that is location of the strong  $K\alpha$  lines of the He-like Na ion. This is precisely the location of the weak residuals discussed above for the other galaxies. If the Ni abundance is also unphysical, then additional errors likely exist in either the Fe L shell lines or in the Ni L shell emission of the MEKAL code. Since much more attention has been devoted to correcting the strong Fe L shell emission lines (e.g. Liedahl et al. 1995; Wargelin et al. 1998; Brown et al. 1998), it is possible that the neglected Ni L lines require some adjustments as well.

However, as we show in section 5.3, temperature gradients may partially explain the Na abundance inferred for NGC 4636.

## 4 ANALYSIS OF INDIVIDUAL LINE BLENDS WITH ASCA

We have shown that the important constraints from the broad-band spectral fitting are largely determined from the data near 1 keV which are dominated by emission lines from the Fe L shell. Although good fits for these galaxies are obtained for multiphase models using the MEKAL plasma code, it is instructive to examine whether the ASCA data outside the Fe L region of the spectrum also favor multiphase models over isothermal models. In particular, the emission lines from the  $K\alpha$  transitions of the He-like and H-like ions of Si and S provide constraints on the temperature complementary to the Fe L emission lines. These emission lines have the advantage that they are well separated in energy from the strong Fe L shell lines and their properties are relatively simple and thus are known to much higher accuracy than the Fe L lines .

## 4.1 Deduced line properties from ASCA data

For our study of the Si and S line blends we must pay special attention to the calibration problem in the energy response near 2.2 keV owing to the optical constants in the XRT (Gendreau & Yaqoob 1997). Although the ARF files generated with the standard software (see section 2) correct for much of this problem, there are low-level residuals extending throughout the energies of the key Si and S lines. For compactness of presentation, the results we present for the joint SIS0+SIS1 fits for NGC 1399 (8003800) and NGC 4472 (60029000) refer to one observation sequence in each case.

We focus our analysis of individual line blends on the SIS data because, unlike the GIS, the SIS is able to resolve the He-like and H-like blends of Si and S (see section 3.1). In no instance did we find that constraints on the line properties improved noticeably when incorporating the GIS data into the fits.

Our procedure for obtaining the properties of the line blends commences by fitting a thermal bremsstrahlung model to represent the continuum emission. We desire a measurement of the local continuum near the line blends of interest so that the assumption of a single temperature is reasonable even if the spectrum actually consists of multiple temperature components. However, because of S/N considerations and the finite energy resolution of the SIS we allowed the continuum component to extend over multiple line blends that are nearby in energy.

The line blends of interest were then modeled as gaussians of zero intrinsic width on top of the continuum component. For analysis of the Si and S line blends we fitted the bremsstrahlung model over the open interval (1.7,2.85) keV with gaussian components initially at 1.85 keV (Si XIII), 2.0 keV (Si XIV), 2.45 keV (S XV), and 2.62 keV (S XVI). The energies of the lines were free parameters in the fits. When determining the error bars on the equivalent widths and fluxes for a particular line the energies of the other lines were fixed at their best-fit values. This was done to insure that the other lines did not mix during the error search.

For completeness, when available we also derived properties for the Mg and Ar line blends. The continuum for the Mg XI (He) and Mg XII (H) lines was defined over the open interval (1.23,1.6) keV. For the Ar XVII (He) blend we used the open interval (2.85,5) keV. The properties of the all detected lines are listed in Tables 6 and 7. In Figure 8 we plot the SIS data and best-fitting model over the spectral region used to determine the properties of the Si and S lines for each galaxy. Since the continuum+lines model fit well for each system we do not show the residuals in the figure.

The  $K\alpha$  line blends of the He-like and H-like ions of Si and S are detected for each galaxy except the S XVI blend of NGC 4636. Both the Mg XI and XII  $K\alpha$  line blends are detected for NGC 4636 and NGC 5044 in each SIS; these blends are detected only in the combined SIS data for NGC 1399 and only for Mg XII for NGC 4472. We also detect weak Ar XVII (He) emission in NGC 1399 in both the SIS0 and SIS1.

Generally the line energies computed for the SIS0 and SIS1 agree within their estimated 90% confidence limits. The line equivalent widths (EWs) and fluxes mostly agree within these limits with some notable exceptions: S XIV for NGC 4636 and both S complexes for NGC 1399. The ratios of the

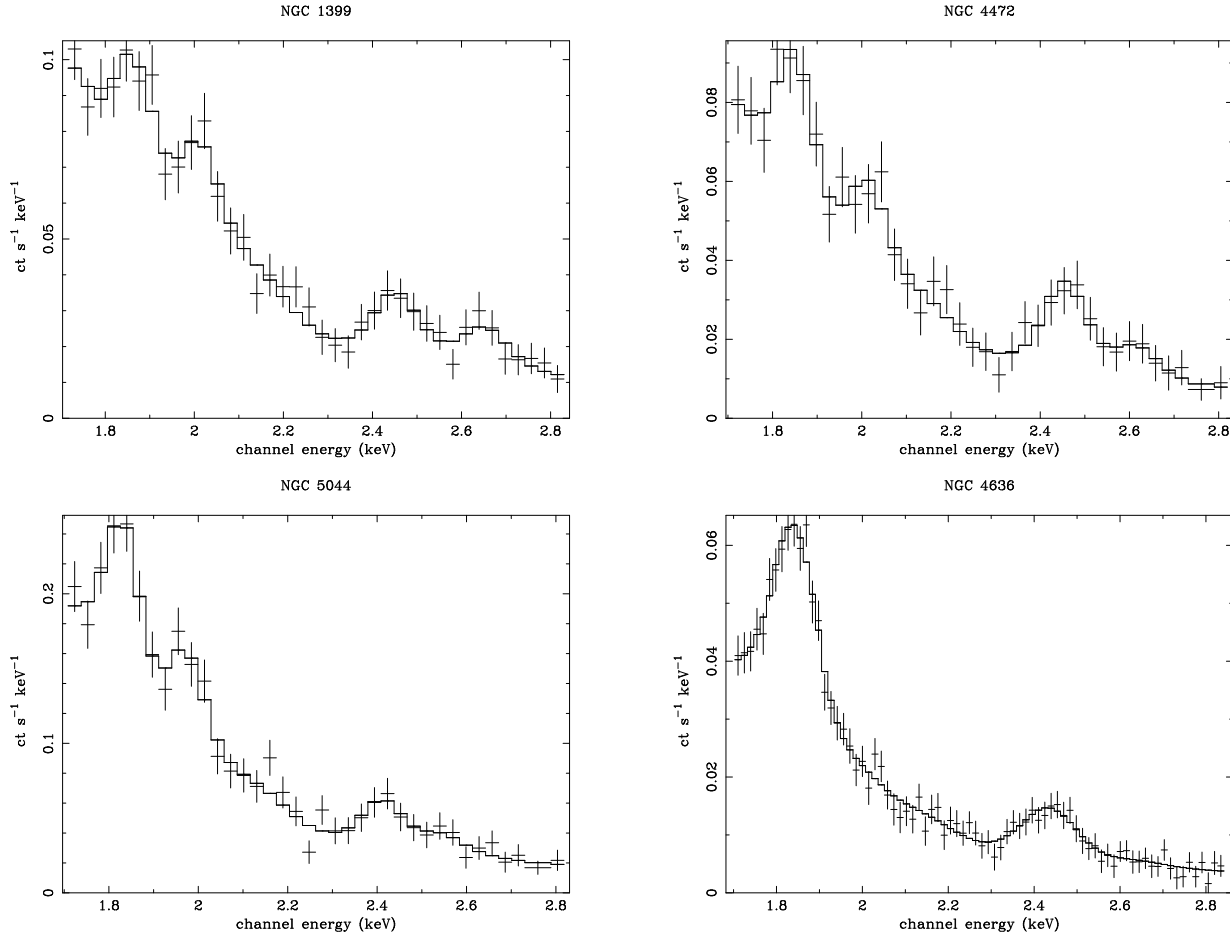


**Figure 8.** ASCA SIS data between energies 1.7 and 2.85 keV for NGC 1399, NGC 4472, NGC 5044, and NGC 4636. Also shown for each galaxy is the best-fitting model consisting of a thermal bremsstrahlung component to represent the continuum emission and four gaussians of zero intrinsic width to model respectively the major  $K\alpha$  emission line complexes of Si XIII, Si XIV, S XV, and S XVI. See Table 6 for the parameters of these emission lines.

H-like/He-like  $K\alpha$  fluxes for both Si and S (Table 7) also agree within the estimated  $2\sigma$  limits for the SIS0 and SIS1.

Therefore, although the marginal agreement (or rather disagreement) at the 90% confidence level for the fluxes computed for the SIS0 and SIS1 may point to underlying systematic errors as discussed above, such errors are mostly blurred by the S/N of these data. As done previously with the broad-band spectral analysis, we shall henceforth focus on analysis of the summed SIS data which essentially averages over the systematic differences in the SIS0 and SIS1 data. (The possible underlying systematic differences between the SIS0 and SIS1 must be regarded as a caveat to any analysis of the emission lines of these galaxies with the ASCA SIS, including the analysis presented in the following section.)

## 4.2 Comparison to isothermal and multiphase models

We compare the equivalent widths and ratios of the Si and S line blends computed using the continuum+gaussian approximation with those predicted by the models obtained from the broad-band spectral fitting. Although our focus is on these lines that are far from the Fe L energy region, we comment on the Mg lines near the end of this section. Ex-

amination of Figure 8 and Tables 6 and 7 reveals substantial Si XIV  $\text{ly-}\alpha$  emission for NGC 1399, NGC 4472, and NGC 5044 with respect to NGC 4636. Similarly, there is significant S XVI  $\text{ly-}\alpha$  emission for NGC 1399 and NGC 4472 (and marginally for NGC 5044) whereas only upper limits are obtained for NGC 4636.

The fact that the Si XIV/XIII and S XVI/XV ratios are comparable for NGC 1399, NGC 4472, and NGC 5044 but are clearly smaller for NGC 4636 indicates that the plasma temperature of NGC 4636 is significantly smaller than the others – a statement that is independent of the Si and S abundances<sup>†</sup>. This demonstrates at least a “zeroth-order” level of consistency between the temperatures derived from the  $K\alpha$  lines of Si and S with those determined largely by the Fe L lines from the broad-band spectral fitting analysis in section 3.

Let us now examine in detail how well the models obtained from the broad-band spectral fitting reproduce the

<sup>†</sup> This insensitivity to the abundance is exact for an isothermal plasma, but it should be noted that for multiphase plasmas like cooling flows there can be a small metallicity dependence for such line ratios (Buote et al. 1998).

**Table 6.** Emission Lines Measured from ASCA Data

	$E$ (keV)	$T$ (keV)	EW (eV)	Flux ( $10^{-5}$ ph cm $^{-2}$ s $^{-1}$ )	Flux ( $10^{-13}$ erg cm $^{-2}$ s $^{-1}$ )
NGC 1399:					
Mg XI (He)	1.38 $^{+0.05}_{-0.03}$	0.99 $^{+0.58}_{-0.31}$	14 $^{+13}_{-11}$	1.82 $^{+1.58}_{-1.43}$	0.40 $^{+0.35}_{-0.32}$
Mg XII (H)	1.49 $^{+0.03}_{-0.05}$	0.99 $^{+0.58}_{-0.31}$	18 $^{+20}_{-15}$	1.96 $^{+1.84}_{-1.61}$	0.47 $^{+0.44}_{-0.38}$
Si XIII (He)	1.87 $^{+0.02}_{-0.01}$	1.09 $^{+0.38}_{-0.24}$	96 $^{+32}_{-29}$	5.05 $^{+1.38}_{-1.37}$	1.51 $^{+0.41}_{-0.41}$
Si XIV (H)	2.01 $^{+0.02}_{-0.01}$	1.09 $^{+0.38}_{-0.24}$	84 $^{+28}_{-26}$	3.52 $^{+1.02}_{-1.03}$	1.13 $^{+0.33}_{-0.33}$
S XV (He)	2.45 $^{+0.02}_{-0.02}$	1.09 $^{+0.38}_{-0.24}$	140 $^{+64}_{-53}$	3.02 $^{+1.06}_{-1.00}$	1.18 $^{+0.42}_{-0.39}$
S XVI (H)	2.65 $^{+0.03}_{-0.03}$	1.09 $^{+0.38}_{-0.24}$	108 $^{+74}_{-65}$	1.74 $^{+0.88}_{-0.97}$	0.74 $^{+0.37}_{-0.41}$
Ar XVII (He)	3.13 $^{+0.07}_{-0.07}$	2.54 $^{+2.23}_{-0.85}$	77 $^{+72}_{-60}$	0.87 $^{+0.69}_{-0.67}$	0.44 $^{+0.35}_{-0.33}$
NGC 4472:					
Mg XII (H)	1.47 $^{+0.02}_{-0.02}$	0.49 $^{+0.14}_{-0.09}$	32 $^{+20}_{-19}$	3.02 $^{+1.53}_{-1.72}$	0.71 $^{+0.36}_{-0.40}$
Si XIII (He)	1.85 $^{+0.01}_{-0.01}$	0.91 $^{+0.37}_{-0.21}$	136 $^{+48}_{-42}$	5.67 $^{+1.48}_{-1.49}$	1.68 $^{+0.44}_{-0.44}$
Si XIV (H)	2.01 $^{+0.02}_{-0.02}$	0.91 $^{+0.37}_{-0.21}$	90 $^{+39}_{-35}$	2.82 $^{+1.01}_{-1.01}$	0.91 $^{+0.32}_{-0.32}$
S XV (He)	2.46 $^{+0.02}_{-0.02}$	0.91 $^{+0.37}_{-0.21}$	244 $^{+100}_{-84}$	3.62 $^{+1.04}_{-1.04}$	1.42 $^{+0.41}_{-0.41}$
S XVI (H)	2.62 $^{+0.05}_{-0.06}$	0.91 $^{+0.37}_{-0.21}$	100 $^{+100}_{-78}$	1.14 $^{+0.86}_{-0.86}$	0.48 $^{+0.36}_{-0.36}$
NGC 4636:					
Mg XI (He)	1.34 $^{+0.01}_{-0.01}$	0.32 $^{+0.03}_{-0.03}$	48 $^{+10}_{-9}$	4.11 $^{+0.67}_{-0.67}$	0.88 $^{+0.14}_{-0.14}$
Mg XII (H)	1.47 $^{+0.01}_{-0.02}$	0.32 $^{+0.03}_{-0.03}$	32 $^{+17}_{-14}$	1.58 $^{+0.69}_{-0.67}$	0.37 $^{+0.16}_{-0.16}$
Si XIII (He)	1.84 $^{+0.00}_{-0.00}$	0.98 $^{+0.26}_{-0.18}$	264 $^{+37}_{-34}$	5.41 $^{+0.47}_{-0.46}$	1.60 $^{+0.14}_{-0.14}$
Si XIV (H)	1.98 $^{+0.03}_{-0.03}$	0.98 $^{+0.26}_{-0.18}$	45 $^{+21}_{-20}$	0.74 $^{+0.31}_{-0.31}$	0.24 $^{+0.10}_{-0.10}$
S XV (He)	2.43 $^{+0.02}_{-0.01}$	0.98 $^{+0.26}_{-0.18}$	228 $^{+61}_{-53}$	1.78 $^{+0.33}_{-0.33}$	0.69 $^{+0.13}_{-0.13}$
S XVI (H)	2.64	0.98 $^{+0.26}_{-0.18}$	25 $^{+37}_{-25}$	0.14 $^{+0.28}_{-0.14}$	0.06 $^{+0.12}_{-0.06}$
NGC 5044:					
Mg XI (He)	1.35 $^{+0.03}_{-0.03}$	0.44 $^{+0.15}_{-0.05}$	20 $^{+11}_{-14}$	6.35 $^{+3.18}_{-4.33}$	1.37 $^{+0.69}_{-0.94}$
Mg XII (H)	1.49 $^{+0.02}_{-0.03}$	0.44 $^{+0.10}_{-0.05}$	36 $^{+16}_{-25}$	7.14 $^{+2.58}_{-4.78}$	1.70 $^{+0.62}_{-1.14}$
Si XIII (He)	1.83 $^{+0.01}_{-0.01}$	0.97 $^{+0.29}_{-0.19}$	115 $^{+34}_{-29}$	10.43 $^{+2.12}_{-2.11}$	3.07 $^{+0.62}_{-0.62}$
Si XIV (H)	1.98 $^{+0.01}_{-0.01}$	0.97 $^{+0.29}_{-0.19}$	108 $^{+32}_{-28}$	7.70 $^{+1.83}_{-1.83}$	2.44 $^{+0.58}_{-0.58}$
S XV (He)	2.42 $^{+0.02}_{-0.02}$	0.97 $^{+0.29}_{-0.19}$	126 $^{+50}_{-46}$	4.59 $^{+1.55}_{-1.55}$	1.78 $^{+0.60}_{-0.60}$
S XVI (H)	2.55 $^{+0.09}_{-0.09}$	0.97 $^{+0.29}_{-0.19}$	54 $^{+56}_{-49}$	1.50 $^{+1.33}_{-1.34}$	0.61 $^{+0.34}_{-0.55}$

Properties of emission lines derived from fitting simple continuum+lines models to the summed ASCA SIS data. The continuum is represented by a thermal bremsstrahlung component and the lines by gaussians of zero intrinsic width. Lines that have the same continuum temperature,  $T$ , are cases where multiple gaussians are joined by one bremsstrahlung component. See text for additional details regarding the model fitting. Quoted errors are 90 per cent confidence on one interesting parameter. Line energies without error bars were fixed at their best-fitting values.

**Table 7.** Line Ratios

	NGC 1399	NGC 4472	NGC 4636	NGC 5044
Si XIV/Si XIII	0.75 $^{+0.58}_{-0.33}$	0.54 $^{+0.45}_{-0.27}$	0.15 $^{+0.08}_{-0.07}$	0.79 $^{+0.44}_{-0.29}$
S XVI/SXV	0.62 $^{+0.78}_{-0.42}$	0.34 $^{+0.49}_{-0.27}$	0.09 $^{+0.23}_{-0.09}$	0.35 $^{+0.64}_{-0.32}$

Ratios of  $K\alpha$  emission lines for the H-like and He-like ions of Si and S using the fluxes from Table 6. Quoted errors represent ratios of 90 per cent confidence lower limits to 90 per cent confidence upper limits and vice versa. Thus, the quoted error ranges reflect larger than a 90 per cent confidence interval and typically correspond to  $\sim 2\sigma$  confidence.

observed Si and S line ratios and equivalent widths. Our method to extract the properties of the Si and S line complexes using a bremsstrahlung component and four zero-width gaussians is a convenient approximation appropriate for the energy resolution of the SIS data. To account for any biases in this procedure we compute the line properties from the models using the same procedure. That is, for each best-fitting isothermal, two-temperature, and cooling flow model listed in Table 4 we simulated a SIS observation (using XSPEC) with an exposure time sufficiently long so that the statistical errors in our derived parameters for

each model are generally  $< 10\%$ . We found that exposure times of  $10^7$ s -  $10^8$ s were satisfactory for this purpose.

In Figure 9 we plot the  $K\alpha$  line ratios Si XIV/XIII and S XVI/XV of the models and data. The equivalent widths of the line complexes are displayed in Figure 10 for the models and data. Note that the error bars on the ratios in Figure 9 for the data are  $\sim 2\sigma$  while the error bars for the equivalent widths in Figure 10 are 90% confidence limits.

Inspection of Figure 9 reveals that the Si and S ratios of each of the three models for NGC 1399 are consistent within the  $2\sigma$  limits. Although all the models are consis-

tent, the cooling flow model best reproduces these ratios. The isothermal model agrees with the Si ratio better than the two-temperature model and vice versa for the S ratio. The equivalent widths (Figure 10) for all of the models are also consistent with the data of NGC 1399 except for the S XVI line blend where the isothermal model under-predicts the equivalent width. In fact, except for the Si XIV line, the isothermal model tends to under-predict the equivalent widths of the lines with respect to the multiphase models.

To facilitate our comparison of equivalent widths we define the quantity,

$$\Delta_{EW} \equiv \sum_i \frac{(EW_i^{data} - EW_i^{model})^2}{\sigma^2}, \quad (1)$$

where  $\sigma$  is the one-sided 68% confidence level of the equivalent widths estimated from the data and the summation runs over the two Si and two S line blends. The purpose of  $\Delta_{EW}$  is to provide a number to indicate the relative agreement of the various models analogously to  $\chi^2$ .

For NGC 1399 we have  $\Delta_{EW} = (1.59, 0.75, 0.30)$  for respectively the best-fitting isothermal, two-temperature, and cooling flow models. That is, the isothermal model clearly shows the most deviations and the cooling flow model agrees better than the two-temperature model. Since each model has comparable emission-weighted temperature, the smaller equivalent widths of the isothermal model are due primarily to the smaller Si and S abundances of the model (see Table 4).

Loewenstein & Mushotzky (1997) have asserted that the Si ratio computed for ASCA SIS data of NGC 1399 is consistent with a isothermal model but is inconsistent with the two-temperature model presented in BF. Our two-temperature models agree well with BF and, as we have just shown, also predict Si ratios that agree with the data. It is true that for the Si ratio the isothermal model gives better agreement than the two-temperature model. However, we have shown this to be misleading since when the S ratio and the equivalent widths of the Si and S line blends are also considered together with the Si ratio we find that the two-temperature and cooling flow models agree much better with the data than does the isothermal model.

The Si and S ratios for each model also agree with the data of NGC 4472. The agreement is good for all models for the Si ratio, but for the S ratio the two-temperature model fares much better than the isothermal case which is only marginally in agreement at the  $2\sigma$  lower limit. With the exception of the Si XIII blend where the agreement is good for all models, the models tend to under-predict the equivalent widths for the Si and S lines though the only actual discrepancy is for the isothermal prediction of S XVI. In terms of  $\Delta_{EW}$  we have (1.47, 1.28, 1.07) for respectively the best-fit isothermal, two-temperature, and cooling flow models. Hence, all models are comparable, though the multiphase models, especially the cooling flow, is the best fit to the Si and S equivalent widths similar to NGC 1399.

For NGC 5044 we find that no model is able to reproduce the Si ratio within the  $2\sigma$  error. The multiphase models, though, give Si ratios in much better agreement with the data than do the isothermal models. The model ratios also tend to be low for S, though the multiphase models are consistent within the errors while the isothermal ratio is in-

consistent. These results for the Si and S ratios suggest that higher temperature gas is needed in the models. The need for additional temperature components is not inconsistent with the broad-band fits since, e.g., even the best cooling flow models are only marginally acceptable in terms of their null hypothesis probabilities (see Table 3).

The equivalent widths of Si and S further support the need for higher plasma temperature components in NGC 5044. All models tend to over-predict the He-like Si XIII and S XV emission while under-predicting the H-like Si XIV and S XVI emission, though the most significant disagreement lies with the isothermal models:  $\Delta_{EW} = (8.38, 2.41, 3.07)$  for respectively the best-fit isothermal, two-temperature, and cooling flow models.

The Si ratio of NGC 4636 is marginally acceptable for the multiphase models and inconsistent for the isothermal model within the  $2\sigma$  errors. If only the relative abundances of the  $\alpha$ -process elements are varied for the two-temperature model (i.e. Na and Ni abundance tied to Fe) then the predicted ratio for the two-temperature model rises to 0.15. This excellent agreement for the two-temperature model is not shared by the corresponding isothermal model with variable relative abundances for only the  $\alpha$ -process elements. All the models predict a value of zero for the S ratio which is consistent with the data.

Only the two-temperature model predicts equivalent widths for each Si and S blend that are at least marginally consistent with the data. The largest deviation is found for Si XIV where the isothermal model produces too small an equivalent width. However, the cooling flow model generally has the most deviations:  $\Delta_{EW} = (2.38, 1.16, 5.48)$  for respectively the best-fit isothermal, two-temperature, and cooling flow models. Similar to the results from the broad-band analysis, the relatively poor performance of the cooling flow for NGC 4636 is probably in large part due to the restriction that the model have relative abundances fixed at their solar values.

The equivalent widths of Si and S and especially the Si ratio give strong support for multiphase gas in NGC 4636 (or, rather, gas hotter than predicted by the isothermal models). Although the broad-band fits slightly favor the two-temperature model (Table 3), the difference in  $\chi^2$  between the isothermal and two-temperature models is not compelling: i.e. the Si and S lines give stronger evidence for multiphase gas in NGC 4636 than do the broad-band fits.

Recently Loewenstein (1998) has argued that the Si XIV/XIII ratio of NGC 4636 is consistent with isothermal gas. From inspection of Figure 4 of Loewenstein we find he derives a value of  $\sim 0.15$  for the Si ratio from the data in excellent agreement with our value for the summed SIS data in Table 7. He also asserts that this ratio is consistent with isothermal gas with a temperature  $\sim 0.75$  keV. As we have shown in Table 4 isothermal models (both MEKAL and RS) with variable relative abundances have temperatures  $\sim 0.66$  keV which, consistent with Loewenstein's figure, cannot produce the Si ratios; note that the isothermal models (both MEKAL and RS) with relative abundances fixed at their solar values do have temperatures near 0.75 keV but their fits are substantially worse and have very poor null hypothesis probabilities (see Table 3). Thus, the Si ratio of NGC 4636 cannot be produced by isothermal models which also best match data over the rest of the ASCA spectrum.

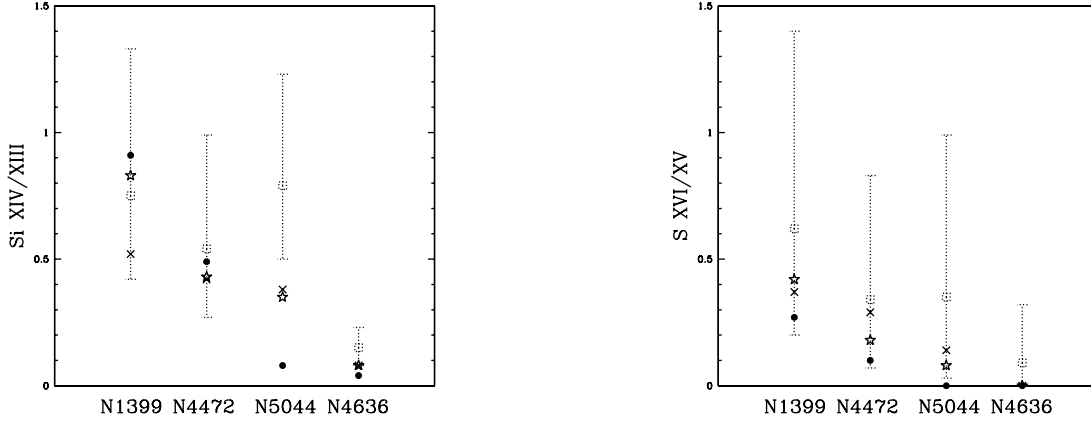


**Figure 9.**  $K\alpha$  line ratios of H-like to He-like ions of Si (left) and S (right) for the ASCA SIS data (dotted) with  $\sim 2\sigma$  error bars (Table 7) plotted along with ratios computed from the best-fit (MEKAL) models of Tables 4 and 5: isothermal (filled circle); two-temperature (crosses); multiphase cooling flow (stars).

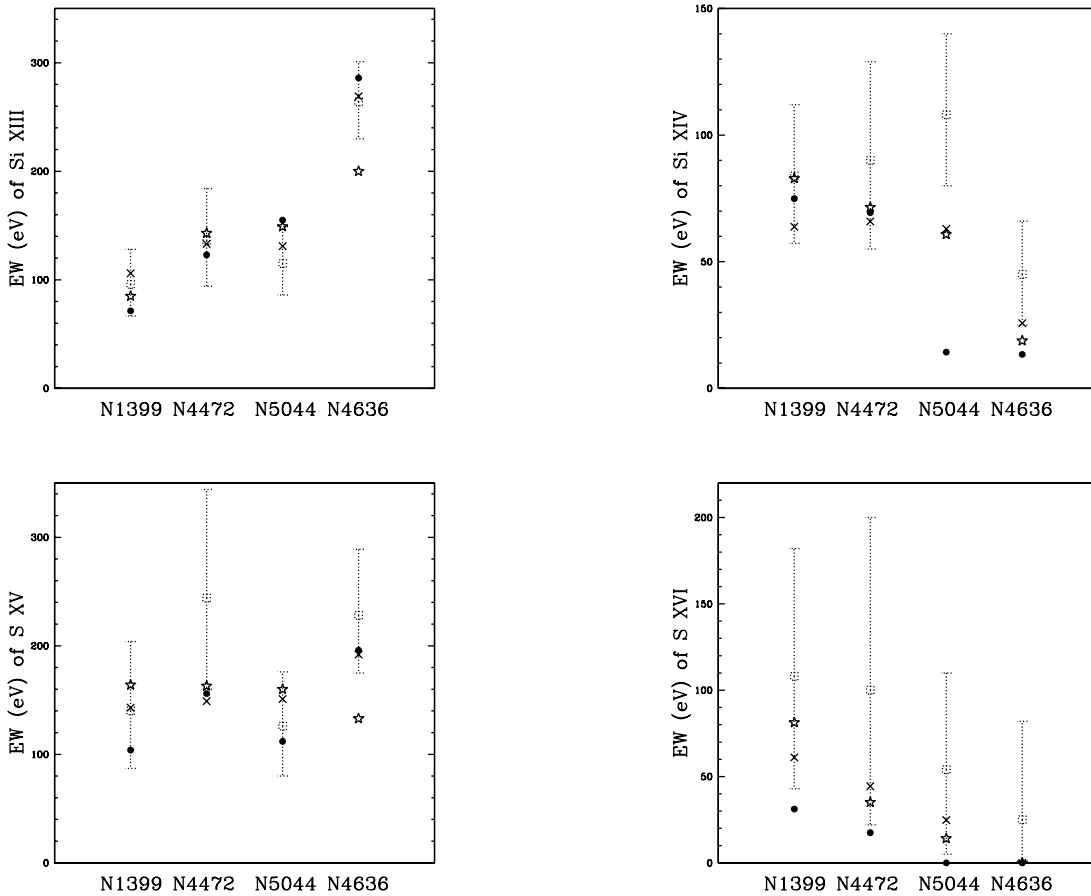


**Figure 10.** As Figure 9 except that the equivalent widths of the lines for the data and models are shown and the error bars represent 90% confidence levels ( $\Delta\chi^2 = 2.71$ ).

We mention that for all of the galaxies the equivalent widths and Mg XII/XI ratios (where available) predicted by the models are mostly consistent with the data within the  $2\sigma$  errors. The most notable discrepancy is for NGC 1399 where the isothermal model substantially under-predicts the

equivalent width of Mg XII while the multi-phase models substantially over-predict the equivalent width.

Hence, for all of the galaxies we find that the line equivalent widths and H-like/He-like ratios for Si and S generally favor multiphase models over isothermal. For NGC 1399 and

NGC 4472 the isothermal models tend to under-predict the equivalent widths which is due to the smaller abundances of those models. The better performance of the multiphase models of NGC 4636 and NGC 5044 is primarily the result of the need for a higher temperature component than present in the isothermal models.

## 5 RADIAL TEMPERATURE GRADIENTS FROM ROSAT

The evidence we have obtained for multiphase gas with approximately solar abundances rests on analysis of the aggregate *ASCA* spectra within a radius of  $\sim 5'$  for each galaxy. The data of these galaxies available from the *ROSAT* satellite (Trümper 1983) do not provide useful “aggregate” spectral constraints over those obtained from the *ASCA* data because of the limited energy resolution ( $\Delta E \sim 500$  eV at 1 keV) and bandwidth (0.1-2.4 keV) of the *ROSAT* Position Sensitive Proportional Counter (PSPC) with respect to *ASCA*. However, the superior spatial resolution of the PSPC (PSF  $\sim 30''$  FWHM) allows the radial variation of the spectra to be probed within the  $\sim 5'$  apertures.

Although the PSPC cannot distinguish very well between complex spectral models of elliptical galaxies, it can provide relatively tight constraints on a model consisting of a single temperature component (e.g. Buote & Canizares 1994; Trinchieri et al. 1994). This is significant if the aggregate (multiphase) spectra within the  $\sim 5'$  *ASCA* apertures can be approximated as a series of isothermal components; i.e. one temperature for each radial bin within the aperture. This is a reasonable approximation if in each radial bin one temperature component dominates the emissivity.

Previous analyses of the PSPC data of these galaxies using isothermal models in radial bins generally have found significant temperature gradients (Forman et al. 1993; David et al. 1994; Trinchieri et al. 1994; Rangarajan et al. 1995; Irwin & Sarazin 1996; Jones et al. 1997). The temperature profiles are qualitatively similar for all of these galaxies: starting from a minimum at the center the temperature rises sharply out to a radius similar to our *ASCA* apertures and then gently declines at larger radii. The abundances also rise and then fall, typically having approximately solar abundances within the radii of our *ASCA* apertures (except for the innermost radial bin) and smaller abundances at larger radii. Excess absorption is not found from analysis of PSPC data of these ellipticals (e.g. section 4 of BF) except by Rangarajan et al. (1995) for the central radial bin of NGC 1399.

This evidence for multitemperature structure with approximately solar abundances within  $\sim 5'$  radii of NGC 1399, NGC 4472, NGC 4636, and NGC 5044 appears to corroborate our single-aperture *ASCA* spectral analysis. We do not expect the spectral models derived from the PSPC data to agree exactly with our *ASCA* models because a single-temperature model for each radial bin may not be an accurate representation. It is our goal in this section to assess the extent to which the temperature profiles derived from the PSPC data agree with the isothermal and multiphase models obtained from our *ASCA* spectral analysis.

## 5.1 Observations and data reduction

We obtained *ROSAT* PSPC observations from the HEASARC archive. The observation sequences are listed in Table 8. The data were reduced using the standard FTOOLS (v4.1) software according to the procedures described in the OGIP Memo OGIP/94-010 (“*ROSAT* data analysis using xselect and ftools”) and the WWW pages of the *ROSAT* Guest Observer Facility (GOF) (See <http://heasarc.gsfc.nasa.gov/docs/rosat/>.)

The events files of each observation were cleaned of after-pulse signals by removing any events following within 0.35 ms of a precursor. We corrected the Pulse Invariant (PI) bins of each data set for spatial and long-term temporal gain variations using the most up-to-date calibration files. For the FTOOL PCECOR, which corrects for the variation in the linearity of the PSPC response, we used the in-flight calibration data for the correction. We then removed large fluctuations in the light curves indicative of scattered light from the Bright Earth, Sun, or SAA. The resulting filtered exposure times are listed in Table 8.

We generated images in the 0.5-2 keV band from the reduced PCPC data of each galaxy. Within the radii defined by the apertures used in our *ASCA* analysis (see section 2) the surface brightness distributions appear mostly symmetrically distributed about the center of each system with the possible exception of NGC 4472 which has a weak enhancement in the surface brightness approximately 2.5 arcminutes SE of the center. (We also confirm the N-S asymmetry in the surface brightness at distances larger than our *ASCA* radii for NGC 1399 as noted by Jones et al. 1997.)

For each galaxy we extracted spectra in a series of radial bins centered by eye on each galaxy center. The bin sizes were chosen to agree with those of Jones et al. (1997) for NGC 1399, Irwin & Sarazin (1996) for NGC 4472, Trinchieri et al. (1994) for NGC 4636, and David et al. (1994) for NGC 5044. The largest radial bin used for each galaxy has inner radius smaller than the radius of the corresponding aperture used in our *ASCA* analysis.

We regrouped the PI bins of each spectrum so that each group had at least 20 counts as done for the *ASCA* data (see section 2). We generated ARF files for the spectrum of each radial bin using the FTOOL PCARF being careful to correctly assign the deltax and delty keywords as described on the *ROSAT* GOF WWW pages. The RMF files were taken from the HEASARC database and used for each galaxy according to when the galaxy was observed: pspcb\_gain1.256.rmf for NGC 1399 and NGC 5044; pspcb\_gain2.256.rmf for NGC 4472 and NGC 4636. Similar to the *ASCA* data analysis, the response matrix for each PSPC spectrum is the product of the RMF and ARF files.

Finally, we obtained background spectra from source-free regions at large off-axis radii similar to those used in the previous *ROSAT* studies. To correct for exposure differences between source and background spectra we multiplied the background spectra by a constant factor representing the ratio of effective exposures at the position of the given source annulus to that of the background.

**Table 8.** *ROSAT* PSPC Observations

	NGC 1399	NGC 4472	NGC 4636	NGC 5044
Sequence	rp600043n00	rp600248n00	rp600016n00	rp800020n00
Exposure (ks)	23.4	25.4	10.8	24.3

The exposures include time filtering.

**Table 9.** *ROSAT* PSPC Spectral Properties of Central and Outermost Radial Bins

Radius (arcmin)	$N_{\text{H}}$ ( $10^{21}$ cm $^{-2}$ )		$T$ (keV)		$Z$ ( $Z_{\odot}$ )		Goodness-of-Fit ( $P/\chi^2/\text{dof}$ )	
	0.2-2 keV	0.5-2 keV	0.2-2 keV	0.5-2 keV	0.2-2 keV	0.5-2 keV	0.2-2 keV	0.5-2 keV
NGC 1399:								
0-1	$0.15^{+0.03}_{-0.03}$	$1.05^{+0.66}_{-0.51}$	$0.91^{+0.03}_{-0.03}$	$0.81^{+0.06}_{-0.07}$	$0.51^{+0.14}_{-0.10}$	$0.30^{+0.10}_{-0.07}$	0.11/145.8/126	0.38/104.9/101
4-6	$0.11^{+0.03}_{-0.03}$	$0.20^{+0.58}_{-0.20}$	$1.49^{+0.13}_{-0.10}$	$1.46^{+0.18}_{-0.20}$	$0.81^{+0.37}_{-0.23}$	$0.70^{+0.63}_{-0.42}$	0.61/133.9/139	0.84/95.3/110
NGC 4472:								
0-1	$0.07^{+0.03}_{-0.03}$	$0.58^{+0.70}_{-0.58}$	$0.87^{+0.02}_{-0.02}$	$0.83^{+0.05}_{-0.05}$	$1.12^{+0.41}_{-0.24}$	$1.62^{+2.37}_{-0.64}$	0.12/146.3/127	0.23/111.0/101
4-7	$0.27^{+0.34}_{-0.14}$	$1.20^{+0.94}_{-0.72}$	$1.34^{+0.07}_{-0.06}$	$1.20^{+0.13}_{-0.14}$	$2.57^{+4.16}_{-1.30}$	$0.98^{+1.38}_{-0.49}$	0.53/137.9/140	0.63/104.5/110
NGC 4636:								
0-1	$0.15^{+0.05}_{-0.06}$	$0.92^{+1.04}_{-0.82}$	$0.64^{+0.02}_{-0.02}$	$0.58^{+0.06}_{-0.08}$	$0.56^{+0.34}_{-0.17}$	1.0(> 0.5)	0.11/119.7/102	0.05/100.9/79
4-6	$0.10^{+0.18}_{-0.10}$	$1.04^{+2.48}_{-1.04}$	$0.96^{+0.06}_{-0.06}$	$0.88^{+0.13}_{-0.19}$	1.5(> 0.6)	1.7(> 0.5)	0.77/67.8/77	0.82/43.6/53
NGC 5044:								
0-1	$0.40^{+0.04}_{-0.04}$	$1.54^{+0.65}_{-0.48}$	$0.81^{+0.01}_{-0.01}$	$0.71^{+0.04}_{-0.05}$	$0.72^{+0.17}_{-0.12}$	$0.69^{+0.39}_{-0.16}$	0.01/193.7/152	0.05/149.9/123
5-6	$0.47^{+0.17}_{-0.13}$	$0.32^{+0.55}_{-0.32}$	$1.24^{+0.08}_{-0.07}$	$1.27^{+0.11}_{-0.12}$	$0.87^{+0.61}_{-0.31}$	$0.84^{+0.86}_{-0.42}$	0.80/103.9/117	0.90/79.0/96

Results of fitting a single absorbed MEKAL model to the PSPC spectra over the energy ranges 0.2-2 keV and 0.5-2 keV for the central radial bin and outermost radial bin (which overlaps the *ASCA* SIS aperture) for each galaxy. Quoted errors are 90% confidence on one interesting parameter ( $\Delta\chi^2 = 2.71$ ).

## 5.2 Spectral analysis of PSPC data

For each galaxy we fit a single absorbed MEKAL model to the 0.2-2 keV PSPC spectrum of each radial bin. In Table 9 we list the results for the central radial bin and outermost radial bin for each galaxy. The column densities and temperatures agree with previous studies within our 90% confidence limits. As expected, the plasma code differences are most pronounced for the abundances which do show significant disagreement in some cases; e.g. Irwin & Sarazin obtain  $Z = 0.4Z_{\odot}$  in the  $0' - 1'$  bin which is  $\sim 1/3$  the value we obtained from the MEKAL fit.

In all we are able to reproduce to reasonable accuracy the rising temperature gradients found in previous studies within the radii defined by our *ASCA* SIS apertures considering that we use the MEKAL plasma codes whereas previous studies used RS. We also find abundance gradients similar to previous studies. It should be mentioned that the abundances rise and then fall for NGC 1399 and NGC 5044 within the inner and outer apertures listed in Table 9; i.e. the abundance reaches a maximum of  $Z \sim 1.5Z_{\odot}$  for  $r = 2' - 4'$  for NGC 1399, and for NGC 5044 the maximum of  $Z \sim 1Z_{\odot}$  is achieved at  $r = 2' - 3'$ .

Let us define the temperature of the central bin as  $T_{\text{in}}$  and the temperature of the outer bin as  $T_{\text{out}}$ . The values of  $T_{\text{in}}$  and  $T_{\text{out}}$  listed for the 0.2-2 keV fits in Table 9 qualitatively agree with respectively the values of  $T_c$  and  $T_h$  that we derived for the two-temperature models fitted to the *ASCA* spectra (Table 4). The values of  $T_{\text{in}}$  tend to exceed  $T_c$  and actually agree better with the emission-weighted temperatures of the cooling flow models for NGC 1399, NGC 4472, and NGC 5044 (see section 3.3.4). The radially-averaged abundances of the PSPC fits agree, within their large errors, with

the 1-2 solar abundances of the two-temperature and cooling flow models obtained from the *ASCA* data.

The column densities in the central radial bins determined from 0.2-2 keV fits to the PSPC spectra do not exceed the Galactic columns in stark contrast to the excess absorption demanded by the colder components of the multiphase *ASCA* models. This well-known discrepancy in  $N_{\text{H}}$  between *ROSAT* and *ASCA* studies has been discussed in the context of ellipticals by BF (see their section 4). The origin of this discrepancy is still controversial as it may be due to a calibration error in one of the instruments, or it may be an artifact of the models used to fit the data.

We have re-examined this issue using these *ROSAT* PSPC data. In every case the isothermal model has the worst fit in the central bin for each galaxy and has a formally marginal  $\chi^2$  null hypothesis probability  $\sim 0.1$  ( $\sim 0.01$  for NGC 5044). Moreover, in the central bin  $N_{\text{H}}$  actually tends to be *less* than the Galactic value, especially for NGC 1399 and NGC 5044. That is, a isothermal MEKAL plasma modified by Galactic absorption does not produce enough X-ray emission at the lowest energies in the 0.2-2 keV PSPC band.

If this excess soft X-ray emission is due to other temperature components, then we would expect that the parameters derived from fitting an isothermal model should depend on the energy range over which the model is fitted. When restricting the fits to the energy range 0.5-2 keV we indeed find significant differences in the isothermal model parameters of the central bins for NGC 1399 and NGC 5044 (see Table 9). The most substantial change is for the column densities: NGC 1399 and NGC 5044 require excess absorption that agrees much better with the multiphase models derived from the *ASCA* data. (Using somewhat different arguments, Rangarajan et al. 1995 also found excess ab-

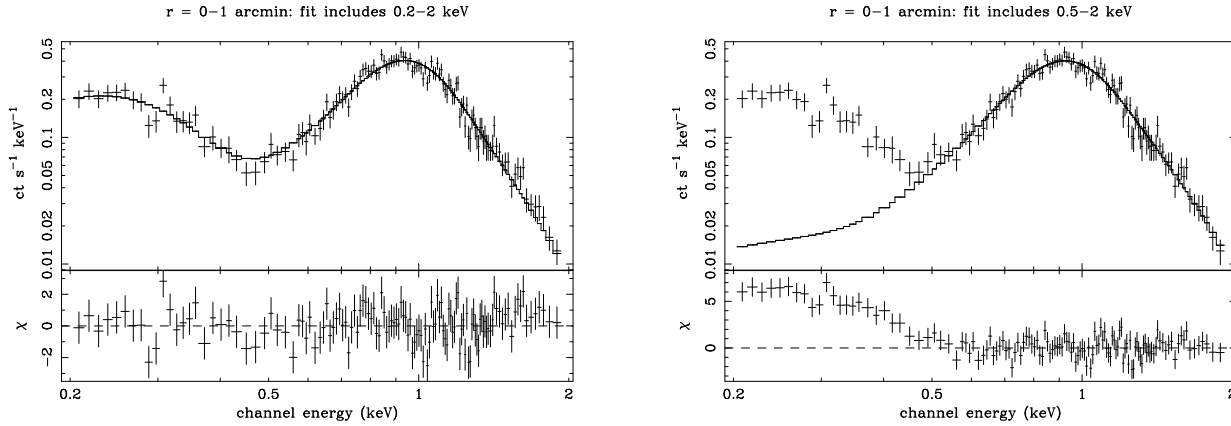


**Figure 11.** Absorbed MEKAL models fit to the *ROSAT* PSPC data of the central radial bin ( $r = 0'-1'$ ) and the outer radial bin ( $r = 4'-6'$ ) of NGC 1399. The left panel shows the result of fitting the entire 0.2-2 keV energy range while the right panel shows the result of fitting only the 0.5-2 keV energy range. (The best-fitting model parameters are listed in Table 9.)

sorption at the center of NGC 1399 in the PSPC data.) The slightly smaller temperatures also agree better with the two-temperature *ASCA* models. Finally, the quality of the fits is also improved most for these galaxies when fitting only to 0.5-2 keV. NGC 4636 and NGC 4472 appear to follow similar trends but their changes for  $N_{\text{H}}$  and  $T_{\text{in}}$  are not as significant.

These effects occur only for the central radial bin of each galaxy. Although some hints of these model differences due to fitting over different energy ranges exist in the second radial bins, the differences diminish rapidly with increasing radius. In particular, for the outer bins listed in Table 9 the column densities, temperatures, and abundances do not change within their 90% confidence limits for NGC 1399 and NGC 5044 when restricting the fits to 0.5-2 keV. When fitted over the restricted energy range of 0.5-2 keV the column densities for the outer bins of NGC 4472 and NGC 4636 become very uncertain. Although the column density for NGC 4636 is consistent with no change, some excess  $N_{\text{H}}$  is implied within the 90% confidence limit for NGC 4472.

The spectra of the central and outer bins are therefore qualitatively different for each galaxy (see Figure 11). Focusing our attention on NGC 1399 and NGC 5044 we see that the outer bin is very consistent with isothermal gas with Galactic absorption (regardless of the energy range fitted). For the central bin of these systems the marginal quality of the fits over 0.2-2 keV coupled with the significant differences in model parameters when confining the fits to 0.5-2 keV implies that the isothermal model is inadequate at the centers. As the panels in Figure 11 vividly demonstrate, the isothermal model with excess absorption which best describes the 0.5-2 keV spectrum under-predicts the emission at lower energies. The excess emission at lower energies is consistent with the existence of additional lower temperature components.

Hence, the PSPC spectra (in particular for NGC 1399 and NGC 5044) indicate significant excess absorption for the central radial bin which decreases rapidly with increasing radius. The central bins also have the coldest temperatures and thus excess absorption is tied to the coldest temperature components. These results concur with the multiphase models obtained from the “single-aperture” analysis of the

*ASCA* data in sections 3.3.3 and 3.3.4. Moreover, the temperatures of the central and outer bins of the PSPC data agree reasonably well with those of the *ASCA* multiphase models. Though the abundances derived from the PSPC data are uncertain, they are approximately solar and are consistent with the multiphase *ASCA* models.

### 5.3 Simulated *ASCA* observations of *ROSAT* PSPC models

We have shown that there is good overall agreement between the multiphase models obtained for the *ASCA* data and the radial temperature profiles obtained by representing the *ROSAT* PSPC spectra as a series of isothermal models as a function of radius within the radii defined by the *ASCA* apertures. These temperature gradients implied by the PSPC, however, appear to be very inconsistent with the isothermal *ASCA* models for NGC 1399 and NGC 5044. Owing to the larger uncertainties for NGC 4472 and NGC 4636, the PSPC temperature gradients do not clearly favor any of the *ASCA* models over another.

We would like to better assess the extent to which the temperature gradients inferred from the PSPC data favor the multiphase *ASCA* models. Although joint fitting of the PSPC and *ASCA* data, as mentioned above, is not useful, an approach that takes advantage of the spatial resolution of the PSPC is to construct a model for each galaxy that is the sum of the isothermal models within the *ASCA* aperture. This composite model can then be fitted directly to the *ASCA* data. The only free parameters are the total normalization and the redshifts (because of the calibration issues discussed in section 3.3.1).

By summing the best-fitting isothermal models over the radial bins within the *ASCA* aperture, we constructed composite PSPC models for each system; in Table 10 we list the parameters of NGC 1399 for illustration. We use the PSPC models derived from fitting the restricted energy range 0.5-2 keV since the isothermal approximation is better suited for the central bin of each galaxy for this energy range as discussed above. Upon fitting these models to the *ASCA* SIS data we obtain good qualitative fits over the whole SIS energy range for NGC 1399 and NGC 5044. For each of these

**Table 10.** Radial Variation of Isothermal Models of the *ROSAT* PSPC data of NGC 1399

Radius (arcmin)	$N_{\text{H}}$ ( $10^{21} \text{ cm}^{-2}$ )	$T$ (keV)	$Z$ ( $Z_{\odot}$ )	$EM$ ( $10^{-17} n_e n_p V / 4\pi D^2$ )
0-1	1.05	0.81	0.30	3.65
1-2	0.22	1.35	1.10	0.83
2-4	0.34	1.44	1.11	1.90
4-6	0.20	1.46	0.70	2.04

Best-fitting absorbed MEKAL model for the PSPC data of each radial bin of NGC 1399. Only the energies 0.5-2 keV are included in these fits which is most important for the central bin as discussed in section 5.2. (See Table 9 for errors on the parameters of the central and outer bins.)

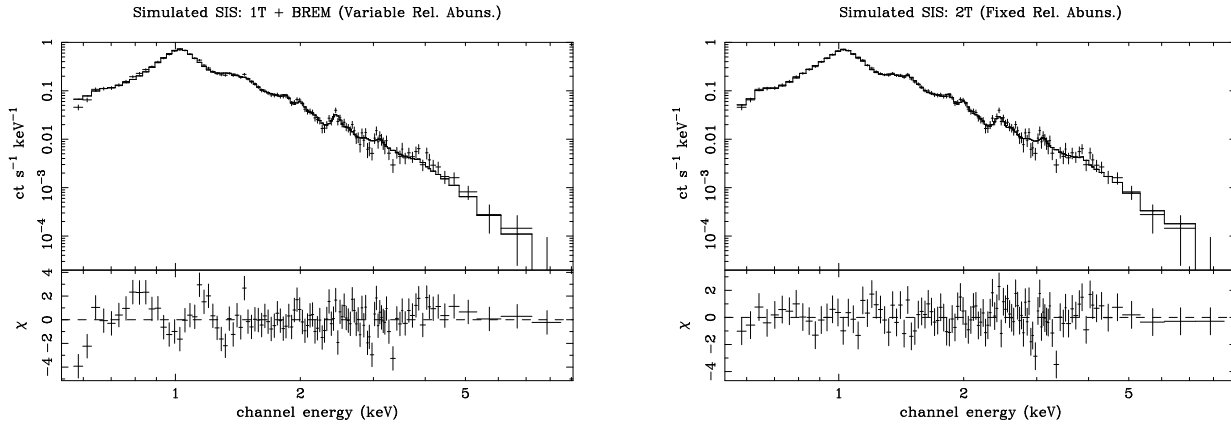


**Figure 12.** Simulated ASCA SIS data of NGC 1399 constructed by summing the radially varying isothermal models obtained from the *ROSAT* PSPC data. The parameters of the composite PSPC models are listed Table 10 except that normalizations are rescaled to match the real ASCA data. The best-fitting 1T+BREM model with variable relative abundances (left) and two-temperature model with relative abundances fixed at their solar values (right) are shown. Both models use the MEKAL plasma code.

galaxies there is a substantial residual near 1 keV which prevents a good formal fit; this residual can be largely removed in each case by changing the individual temperatures of the composite PSPC model within their 90% errors.

Agreement can not be so easily achieved with NGC 4472 and NGC 4636 because, in addition to residuals near 1 keV similar to NGC 1399 and NGC 5044, the PSPC models are clearly deficient in emission above  $\sim 3$  keV. This is not surprising since the limited bandwidth of the PSPC does not allow strong constraints on components (from plasma or discrete sources) which have temperatures  $\gtrsim 3$  keV. Upon adding a bremsstrahlung model to the PSPC model of NGC 4636 the fit improves substantially. Interestingly, the residuals of the fit of this PSPC+BREM model for NGC 4636 are almost identical in shape to those of the cooling flow model fit to the ASCA data in Figure 7.

Perhaps a more interesting comparison of the *ROSAT* and ASCA models is achieved via simulation. That is, for each of the composite isothermal PSPC models we simulate an ASCA SIS observation appropriate for each galaxy; i.e. the same exposure and response as the total summed SIS data (see section 2). (Prior to each simulation the PSPC models are re-scaled to best match the flux of the SIS data though the relative normalizations of the individual components are preserved.) We then analyzed these simulated data analogously to the real ASCA data as done in section 3. Our goal is to examine whether fitting these simulated ASCA data can reproduce in detail the rich behavior found when fitting the real ASCA data.

In Figure 12 we plot the simulated SIS data for NGC

1399 with the best-fitting isothermal and two-temperature models. The isothermal model consists of an absorbed MEKAL model with variable relative abundances and a bremsstrahlung component modified by Galactic absorption. This 1T+BREM model delivers a marginally unacceptable fit to the simulated SIS data:  $P = 10^{-3}$ ,  $\chi^2 = 181.1$  for 127 dof. The residuals near 1 keV are very similar to those in Figure 2 for the real SIS data, though of somewhat smaller magnitude. (Note that the 1T+BREM model with relative abundances fixed at their solar values is a considerably worse fit ( $P = 2 \times 10^{-5}$ ) and has larger residuals near 1 keV in better agreement with Figure 2.) The best-fitting temperature,  $T = 1.20$  keV, and Fe abundance,  $Z_{\text{Fe}} = 0.39Z_{\odot}$ , are very similar to those determined from the real ASCA data (Table 4); the column density,  $N_{\text{H}} = 0.13 \times 10^{21} \text{ cm}^{-2}$  is somewhat smaller. Moreover, the Ne abundance is zero for this 1T+BREM fit and the O and Mg abundances are  $\sim 1/2$  that of Fe.

The two-temperature (Figure 12) and multiphase cooling flow models are excellent fits to the simulated SIS data of NGC 1399 and also have parameters in good overall agreement with those determined from the real ASCA data (Tables 4 and 5):  $P = (0.59, 0.48)$ ,  $\chi^2 = (126.6, 132.3)$  for dof = (131,132) for the 2T and CF+1T model respectively. (Both models have relative abundances with respect to Fe fixed at their solar values and note that a bremsstrahlung component is not included since it does not improve the fits in either case.) The values of  $T_c = 0.73$  keV and  $T_h = 1.36$  keV for the 2T model and  $T = 1.36$  keV for the cooling-flow model agree reasonably well with the real ASCA fits.

We also reproduce the Galactic columns on the hotter components and excess absorption on the colder components, though the excess is still a factor of two below the values listed in Table 4 and 5 for NGC 1399. Both the cooling-flow and two-temperature models give  $Z = 0.73Z_{\odot}$  which is about half that obtained from the actual *ASCA* data. However, this is consistent with the PSPC model listed in Table 10 but should not be considered “real” in particular because the low abundance of the inner bin is probably an artifact of fitting an isothermal model to a spectrum composed of multiple temperature components.

The fits to the simulated SIS data of NGC 5044 behave analogously to NGC 1399 and essentially reproduce the isothermal and multiphase results of fitting the real *ASCA* data. The 1T+BREM models, though, deserve special mention since we find that fitting the simulated SIS data requires a Ne abundance of  $\sim 0.9$  solar and a Ni abundance of  $\sim 1$  solar. The Ne and Ni abundances are very different from Fe (0.3 solar) and allowing them to be free parameters significantly improved the fits as also found when fitting the real *ASCA* data. Thus, these peculiar abundances for the 1T+BREM models do not have to be explained by problems with the MEKAL plasma code.

As expected, the results for NGC 4472 are similar to NGC 1399 and NGC 5044 except that the derived temperatures are lower than obtained from the real *ASCA* data which can be attributed to the deficiency in emission above  $\sim 3$  keV mentioned above. On the other hand, we find that fitting the simulated SIS data for NGC 4636 gives results very similar to those found for NGC 1399 and NGC 5044 except that the 1T model with variable relative abundances is an acceptable fit; unlike the real *ASCA* data, we do not require a bremsstrahlung component for the PSPC models consistent with the deficiency of emission above 3 keV mentioned above. For the most part the parameters derived for the 1T model agree very well with those listed in Table 4 for the 1T+BREM fits to the real *ASCA* data. Even super-solar Na abundance is required, though the best-fit value of 5.9 solar is less than that listed in Table 4.

In contrast to the broad-band fits of the real *ASCA* data of NGC 4636, the two-temperature models are much better fits to the simulated *ASCA* SIS data than the isothermal models and they are not improved significantly when allowing for variable relative abundances. The best-fitting temperatures of the 2T model actually agree well with those found for the real data in Tables 4 and 5; i.e.  $T_c = 0.56$  keV and  $T_h = 0.81$  keV. Although the best-fitting abundance ( $Z = 1.16Z_{\odot}$ ) is larger than that inferred from the real data, there is considerable leverage in the abundance errors in the PSPC models to resolve this discrepancy. Similarly, excess absorption is implied for both components (similar amounts on each component) of the 2T model, much of which can be reduced within the errors of 0.5-2 keV PSPC fits (see Table 9). Overall the fits of the multiphase models to the simulated *ASCA* data of NGC 4636 behave quite similarly to the fits of the real (and simulated) *ASCA* data of the other galaxies. It is very likely that the emission above  $\sim 3$  keV lacking in the *ROSAT* PSPC isothermal models of NGC 4636 accounts for the differences in the multiphase fits to the real and simulated SIS data.

In conclusion, the temperature gradients constructed by radially varying isothermal models of the *ROSAT* PSPC

data are very consistent with the *ASCA* data of NGC 1399, NGC 4472, and NGC 5044 and strongly favor multiphase models of the hot gas in these systems. Our analysis also shows that many of the peculiar abundances derived for the isothermal models of the real *ASCA* data (Table 4) of all the galaxies can be produced by forcing an isothermal model to fit the multiphase spectrum generated by the composite PSPC models. Although the PSPC models suggest the spectral properties of NGC 4636 are quite similar to the other galaxies, strong conclusions cannot be drawn from the radially varying isothermal models of the PSPC data of NGC 4636 and NGC 4472 since they fail to produce the *ASCA* emission above  $\sim 3$  keV.

## 6 DISCUSSION

### 6.1 Evidence for a “Standard Model”?

As remarked in the Introduction most previous studies of ellipticals based on *ASCA* data within a single aperture find that the spectra of these objects are well represented by a component of isothermal hot gas and (if needed) a high temperature bremsstrahlung component to account for possible emission from discrete sources. The evidence for this “Standard Model” is reviewed by Loewenstein & Mushotzky (1997) and Loewenstein (1998). These review articles go further and assert that the  $K\alpha$  emission line ratios Si XIV/Si XIII favor the isothermal models obtained from broad-band spectral fitting and are at best marginally consistent with the multiphase models described in BF.

The accumulated body of evidence from our X-ray analysis of these galaxies strongly favors multiphase models for the hot gas over isothermal models. First, in every case the broad-band spectral fits of the *ASCA* data within a single aperture rule out the isothermal models having relative abundances with respect to Fe fixed at the solar values. Even if the relative abundances are allowed to vary the isothermal models remain poor fits for NGC 1399, NGC 4472, and NGC 5044 especially when the MEKAL model (with its superior modeling of the Fe L shell transitions with respect to RS) is used. The multiphase models with relative abundances fixed at their solar values provide superior fits to these galaxies. (The two-temperature model for NGC 4636 is also a slightly better fit though it requires variable relative abundances.)

We have shown in section 4 that isothermal models generally under-predict the equivalent widths of the Si and S lines of NGC 1399, NGC 4472, NGC 5044, and NGC 4636 while much better agreement with the *ASCA* data is provided by multiphase models. The multiphase models, as a whole, also better describe the measured Si XIV/Si XIII and S XVI/XV ratios. Even for NGC 4636, which displays the smallest improvement for the two-temperature model over the isothermal model for the broad-band spectral fits (section 3), the line ratios and equivalent widths of Si and S clearly favor the two-temperature model. Hence, whereas the previously cited review articles found support for isothermal models using only the Si ratio, we find that consideration of both the ratios and equivalent widths of the Si and S line blends strongly favors the multiphase models.

Our final evidence is obtained by exploiting the superior spatial resolution of the *ROSAT* PSPC. The PSPC data

are generally consistent with a series of isothermal models which vary with radius within the apertures used for analysis of the *ASCA* data. Using different approaches (sections 5.2 and 5.3) we find that the temperature gradients inferred from the *ROSAT* PSPC data (section 5) are inconsistent with the isothermal models derived from fitting the *ASCA* data within a single-aperture but are very consistent with the multiphase models, especially for NGC 1399 and NGC 5044.

In light of this evidence we would argue that the Standard Model for these brightest ellipticals should be revised as follows: (1) the spectra within the *ASCA* apertures consist of at least two temperature components for the hot gas; (2) the temperature declines towards the center as indicated by the temperature profiles deduced from the *ROSAT* PSPC; (3) the Fe abundances are approximately 1-2 solar and the relative abundances of the elements with respect to Fe are also consistent with solar; (4) excess absorption above the Galactic value is indicated for the colder temperature components which declines rapidly with increasing radius until the absorption is consistent with the Galactic value for the hotter temperatures at the outer radii; (5) the *ASCA* spectra are also consistent with a bremsstrahlung component arising from discrete sources contributing  $\lesssim 0.1\%$  to the total emission measure.

To escape this version of a Standard Model (at least for these brightest ellipticals) one has to invoke serious errors in the plasma codes and/or the calibration of the *ASCA* SIS. (Of course, errors of such magnitude would render invalid all existing results of significance for both isothermal and multiphase models.) The relative calibration of *ASCA* and the *SAX* satellite has been examined in detail and no serious discrepancies have been found apart from the small differences in the energy response below 1 keV discussed in section 3.3.1 (e.g. Orr et al. 1997).

The accuracy of the Fe L shell emission lines in the plasma codes has been tested previously by Hwang et al. (1997) who used *ASCA* SIS data to show that the Fe abundance of M87 deduced from analysis of the Fe K shell lines near 6.5 keV is very consistent with that inferred from broad-band spectral fitting that includes the Fe L shell emission lines. Since the average temperature of M87 is  $\sim 2$  keV, this consistency test may not be entirely appropriate for normal ellipticals with  $T \lesssim 1$  keV. However, BF tested the accuracy of the Fe L shell lines for normal ellipticals by comparing the temperatures and abundances derived from fitting MEKAL and RS models over a restricted energy region where the Fe L lines dominate the spectrum. These results were then compared to the fits with the Fe L energy region excluded. They found good agreement between the temperatures and abundances in both cases, especially for the MEKAL model.

In our present paper we have found that excellent fits to both the *ASCA* SIS and GIS data are achieved by multiphase models that use the MEKAL plasma code. Comparison of fits using the MEKAL and RS plasma codes shows that, as expected, the MEKAL code is more accurate and also that remaining inaccuracies in the code are most likely insufficient to negate the evidence in support of multiphase models (section 3.2.3). Hence, we do not find any evidence that errors in the plasma codes near the Fe L energy region (or calibration errors) are sufficient to change qualitatively

the evidence for multiphase hot gas with approximately solar abundances presented in this paper.

## 6.2 Implications of solar abundances

Recently Arimoto et al. (1997) have shown that the stellar Fe abundances deduced from optical observations of a large sample of ellipticals are approximately solar when averaged over an effective radius for each galaxy. This agrees quite well with the Fe abundances predicted by the multiphase models computed within the  $r \sim 5'$  *ASCA* apertures of the ellipticals in our sample but is inconsistent with the sub-solar Fe abundances predicted by the isothermal models. Comparable Fe abundances in stars and the hot gas do not reconcile the standard chemical models where the hot gas is enriched by Type Ia supernovae (e.g. Ciotti et al. 1993).

There is preliminary evidence that the Fe abundances deduced from optical data are in fact  $\sim 0.5$  solar when averaged over an effective radius for each galaxy (Loewenstein 1998). If we take the stellar Fe abundances to be 0.5 solar and the Fe abundances in the hot gas to be 1 solar, then using equation (1) of Arimoto et al. (1997) we have that the standard enrichment models require a Type Ia supernovae rate of  $\sim 0.05h_{75}^2$  SNu. This is a factor of 2.6 below the Type Ia SN rate of  $0.13h_{75}^2$  SNu reported by Capallero et al. (1997), although this discrepancy can be reduced below a factor of two if an Fe abundance of 1.2 solar for the hot gas is used instead. Such a modest increase is still consistent with the range of Fe abundances obtained for the multiphase *ASCA* models.

Thus, if the stellar Fe abundances are near 0.5 solar then the Fe abundances of the hot gas predicted by the multiphase models of the *ASCA* data can be produced to within a factor of two by the standard chemical enrichment models (e.g. Ciotti et al. 1991). This small discrepancy essentially disappears if we increase the Fe abundances we have obtained by a factor of 1.44 to reflect the meteoritic solar abundances instead of the photospheric values we have used – see Ishimaru & Arimoto (1997). It should be mentioned that the 1-2 solar abundances for Fe in the hot gas are also consistent with other scenarios involving both homogeneous (Brighenti & Mathews 1998b) and inhomogeneous cooling flows (Fujita et al. 1997).

It is possible that the abundances vary within the relatively large apertures used to analyze the *ASCA* data. In fact, the cooling flow model of NGC 5044 indicates that the colder gas, which must be more centrally concentrated to be consistent with the *ROSAT* temperature profiles, has higher metallicity than the hotter gas. Abundance gradients are also inferred from analysis of radially varying isothermal models of these galaxies with *ROSAT* (see section 5) and with similar models of the *ASCA* data of NGC 5846 (Finoguenov et al. 1998). However, these results in themselves are not compelling since the isothermal approximation need not be valid, especially for the bins near the centers (see Figure 11).

The 1-2 solar Fe abundances predicted by the multiphase models are substantially larger than the values of  $\sim 0.3$  solar typically found for the intra-cluster medium (ICM) in a rich cluster (Fukazawa et al. 1998). If the Fe abundances for these brightest elliptical galaxies in our sample can be extrapolated to the ellipticals formed in rich clus-

ters, then simple models of the chemical enrichment of the ICM by the hot gas expelled from elliptical galaxies in rich clusters can fit the observations if most of the ICM is primordial (e.g. Loewenstein & Mushotzky 1996).

The relative abundances with respect to Fe deduced from the two-temperature models (section 3.3.3) also favor near-solar values and are consistent with the trend discovered by Fukazawa et al. (1998) that the Si/Fe abundance is nearly solar for the least massive systems such as large ellipticals and small groups of galaxies and increases with the temperature of the system to a value of  $\sim 3$  solar for rich clusters. However, the solar Si/Fe abundances indicated by both our two-temperature and cooling flow models imply nearly solar Si abundances for these galaxies which are similar to those found in rich clusters by Fukazawa et al.; i.e. the solar Si abundances predicted by the multiphase models are not consistent with the trend shown in Figure 2 of Fukazawa et al. wherein the Si abundance of ellipticals should have very sub-solar values.

### 6.3 Two-temperature vs. cooling flow models

The two-temperature models tend to provide slightly better broad-band fits to the ASCA spectra than the cooling flow models. The best-fitting cooling flow models, however, predict Si and S line fluxes for NGC 1399 and NGC 4472 that agree with the ASCA SIS data slightly better than the best-fitting two-temperature models. Buote et al. (1998) have shown that two-temperature models are very flexible and, in particular, can approximate to high accuracy a multiphase cooling flow spectrum throughout the ASCA bandpass. With the ASCA data we thus cannot ascertain reliably whether the spectra consist of only two phases or whether the two-temperature models merely provide good approximations to spectra which have a continuum of temperature components.

There are physical models for the hot gas in ellipticals which accommodate only two phases. Brighenti & Mathews (1998a) find that their most successful models of the ROSAT temperature and surface brightness profiles of NGC 4472 require their isothermal cooling flow model be supplemented with hot gas accreted from the surrounding medium. In this scenario the spectra observed within the ASCA apertures of the ellipticals in our sample are the projection of two nearly isothermal components – a colder component arising from the isothermal cooling flow and a hotter component from the accreted hot gas. (A related scenario for galaxy clusters with cD galaxies is sometimes invoked as an alternative to multiphase cooling flow models; e.g. Xu et al. 1998.) The approximately solar abundances deduced from the ASCA data can also be reproduced by such two-temperature models (Brighenti & Mathews 1998b), although the excess absorption (Table 4) is not an obvious prediction of the model. (Note, however, that related models of isothermal cooling flows can produce material that would give rise to excess absorption – Pellegrini & Ciotti 1998).

Another success of the two-temperature model of Brighenti & Mathews (1998a) also highlights a possible problem with the model. The mass estimated from the stellar dynamics within an effective radius ( $R_e$ ) of NGC 4472 is in excellent agreement with the mass inferred from the X-ray data using the two-temperature model. However, for

$r \lesssim 0.1R_e$  the mass inferred from the X-ray analysis is less than that indicated by stars. One explanation for this discrepancy is that magnetic pressure support becomes important at these small radii which must be accounted for in the X-ray analysis. Alternatively, mass drop-out from the cooling flow may need to be considered.

We obtain results for multiphase cooling flow models of the ASCA data of the elliptical galaxies quite analogous to clusters (e.g. Fabian 1994). In particular, excess absorption on the cooling-flow component and Galactic absorption on the ambient hot gas is indicated for NGC 1399, NGC 4472, and NGC 5044. There is a discrepancy between the mass implied by this absorbing material and the amount of cold gas inferred from HI and CO observations (e.g. see BF and Fabian 1994). This is a critical issue for the simple constant-pressure cooling flow model because the inferred absorbing mass is consistent with the mass deposited by the cooling flow over the galaxy lifetime. It is possible that other versions of multiphase cooling flows would have different predictions for mass deposition.

Broad-band spectral fitting of future observations of elliptical galaxies with *Chandra* will be able to distinguish two-temperature and cooling flow models (Buote et al. 1998). With *ASTRO-E* this distinction can be made using only individual K shell emission lines (particularly of oxygen) thus alleviating any remaining concerns at that time about the accuracy of plasma codes in the Fe L shell energy region.

## 7 CONCLUSIONS

We have examined the ASCA and ROSAT spectra of NGC 1399, NGC 4472, NGC 4636, and NGC 5044, which are among the brightest elliptical galaxies in X-rays, to constrain the temperature structure and abundances of the hot gas in these systems. Our principal aim is to determine whether the ASCA spectra are adequately described by isothermal models of the hot gas, and whether such isothermal models fit the ASCA data as well or better than simple multiphase models. These “isothermal” models actually have two components (1T+BREM) consisting of one component of isothermal hot gas (1T) and another component of thermal bremsstrahlung (BREM) presumably arising from discrete sources.

To begin we simultaneously fit isothermal models to the 0.55-9 keV ASCA SIS and 1-9 keV ASCA GIS spectra of each galaxy using the MEKAL and Raymond-Smith (RS) plasma codes to model the hot gas in each system. Each ASCA spectrum is extracted from a region of  $\sim 5'$  radius because the large energy-dependent PSF confuses spatial analysis on scales much smaller than this. As we discuss below, the spatial variation of the X-ray spectra is examined with the ROSAT PSPC data.

In terms of the  $\chi^2$  null hypothesis probability ( $P$ ) the 1T+BREM fits to the ASCA data are of formally poor quality for each galaxy if the relative abundances with respect to Fe in the hot gas are fixed at their solar values. If the relative abundances of the  $\alpha$ -process elements (and others for NGC 5044 and NGC 4636) are allowed to vary for each galaxy, the fits are improved but are still very poor for all of the galaxies except (marginally) NGC 4636.

The Fe abundances inferred from the isothermal models with variable relative abundances are  $\sim 0.3Z_{\odot}$  for NGC 1399, NGC 4472, and NGC 5044 consistent with previous studies; for NGC 4636 a very sub-solar Fe abundance is also obtained with the RS code, though  $Z \sim 0.8Z_{\odot}$  is implied for the MEKAL code when the relative abundances are allowed to deviate substantially from their solar values. The best isothermal fits require abundances of O, Ne, and Mg to be very different from Fe; these abundances are usually required to be near zero except, e.g., for the Ne abundances of NGC 5044 and NGC 4636 which require values greater than solar for the MEKAL code. Ni abundances very different from Fe are indicated for NGC 4636 and NGC 5044. Finally, the marginal fit for the isothermal model of NGC 4636 using the MEKAL model requires the Na abundance to be many times the solar value.

Next we examined whether simple multiphase models fit the *ASCA* data better than the isothermal models. We studied two-temperature models (2T or 2T+BREM) consisting of two components of hot gas and (if desired) a bremsstrahlung component (BREM) for the putative emission from discrete sources. We also examined a simple multiphase cooling flow where gas cools at constant pressure and drops out of the flow at all radii. This model (CF+1T or CF+1T+BREM) consists of one cooling-flow component (CF), one component of isothermal hot gas (1T) with temperature tied to the upper temperature of the CF component, and (if desired) a bremsstrahlung component (BREM).

The two-temperature models provide substantially better fits to the SIS and GIS data than the isothermal models. With the exception of NGC 4636, these superior fits are achieved with the relative abundances with respect to Fe fixed at their solar values. The cooling flow models fit nearly as well as the two-temperature models for NGC 1399, NGC 4472, and NGC 5044. The poor fit of the cooling flow model to NGC 4636 is probably due largely to the limitation in our implementation of the cooling flow model which fixes the relative abundances at their solar values. The multitemperature fits of NGC 1399 and NGC 4472 are improved significantly when a BREM component is added (2T+BREM), though the reduction in  $\chi^2$  is not so large as that observed between the 1T+BREM and 2T cases. For NGC 4636, in contrast, the addition of the BREM component to the 2T and CF+1T models provides a much larger improvement to the fit than observed between the 1T+BREM and 2T cases. The luminosities of these BREM components are consistent with expectations of emission from discrete sources.

Unlike the isothermal models, the Fe abundances predicted by the multiphase models indicate values of  $\sim 1$ -2 solar. For example, the 2T+BREM models give Fe abundances (90 per cent confidence) of  $1.6^{+0.7}_{-0.6}Z_{\odot}$  for NGC 1399,  $2.0^{+2.4}_{-1.0}Z_{\odot}$  for NGC 4472,  $0.6^{+0.1}_{-0.1}Z_{\odot}$  for NGC 5044, and  $0.7^{+0.3}_{-0.2}Z_{\odot}$  for NGC 4636. The multiphase cooling flows also indicate solar Fe abundances:  $1.1^{+0.4}_{-0.2}Z_{\odot}$  for NGC 1399,  $1.3^{+0.1}_{-0.1}Z_{\odot}$  for NGC 4472,  $0.8^{+0.9}_{-0.2}Z_{\odot}$  for NGC 5044, and  $1.0^{+0.4}_{-0.2}Z_{\odot}$  for NGC 4636. An abundance gradient is also implied by the cooling flow model of NGC 5044 since the abundance determined for the isothermal component ( $0.4^{+0.2}_{-0.2}Z_{\odot}$ ) is considerably less than the cooling flow component. Both the two-temperature and cooling flow models for NGC 1399, NGC 4472, and NGC 5044 predict absorption in excess of the Galactic value for the colder gas components in their

respective models while Galactic absorption is indicated for their hotter components. This is consistent with the radial variation of column density found in the cores of some cooling flow clusters (e.g. Fabian 1994).

The key constraints from the broad-band spectral fitting arise from the SIS data near 1 keV where the Fe L shell emission lines dominate. Errors in the plasma codes are also potentially most serious for these Fe L lines (e.g. Fabian et al. 1994; Liedahl et al. 1995). We find, as expected, that the MEKAL code is much more accurate than RS for the important energies  $\sim 0.7 - 1.4$  keV, and thus the MEKAL models should be used in preference to RS especially for elliptical galaxies. By comparing fits using the MEKAL and RS plasma codes we have determined that remaining errors in the modeling of the Fe L lines by these codes are insufficient to qualitatively change our results obtained from the broad-band spectral fitting. Previous studies by Hwang et al. (1997) and BF also find that the temperatures and Fe abundances inferred for ellipticals using *ASCA* data are not overly sensitive to remaining errors in the plasma codes near 1 keV.

We have measured the emission from the  $K\alpha$  line blends of the H-like and He-like ions of Si and S using a simple model of a bremsstrahlung continuum with zero-width Gaussians for the line blends. These local measurements provide additional constraints independent of the Fe L emission on the models obtained from the broad-band spectral fitting. We find that isothermal models generally under-predict the equivalent widths of the Si and S lines of these systems.

The equivalent widths of the multiphase models, in contrast, are much better matches to the *ASCA* data. The ratios Si XIV/Si XIII and S XVI/XV are also generally better described by the multiphase models. Even for NGC 4636, which displays the smallest improvement for the two-temperature model over the isothermal model for the broad-band spectral fits (section 3), the line ratios and equivalent widths of Si and S clearly favor the two-temperature model. Hence, whereas Loewenstein & Mushotzky (1997) and Loewenstein (1998) found support for isothermal models of ellipticals using only the Si ratio, we find that when both the ratios and equivalent widths of the Si and S line blends are considered, the multiphase models are strongly favored.

We examined whether the temperature profiles inferred from the *ROSAT* PSPC data of these galaxies can also distinguish between the isothermal and multiphase models obtained from the single-aperture analysis of the *ASCA* data. Dividing up the PSPC spectrum for each galaxy into a series of radial bins within the apertures defined for the *ASCA* analysis, we fitted single-temperature MEKAL models to each bin. Each galaxy has a qualitatively similar temperature gradient which begins with a minimum temperature at the center and rises to a maximum at the final radial bin which overlaps the *ASCA* radius in very good agreement with previous studies of these galaxies (Forman et al. 1993; David et al. 1994; Trinchieri et al. 1994; Rangarajan et al. 1995; Irwin & Sarazin 1996; Jones et al. 1997).

The temperatures of the central and outer bins agree quite well with the temperatures of the colder and hotter components obtained for the two-temperature and cooling flow models of the *ASCA* data. The abundances, though uncertain, tend to have values near solar. Finally, the central

bins of the PSPC data are not satisfactorily described by the isothermal model and instead suggest multiphase temperature components and absorption in excess of the Galactic value, especially for NGC 1399 and NGC 5044.

We also constructed composite *ROSAT* models by summing up the isothermal models for each radial bin within the *ASCA* apertures. For each composite PSPC model we simulated an *ASCA* SIS observation appropriate for each galaxy. We then fitted isothermal and multiphase models to these simulated SIS data analogously to our procedure for the real *ASCA* data.

These composite PSPC models are very consistent with the *ASCA* data of NGC 1399 and NGC 5044 and strongly favor multiphase models of the hot gas in these systems. The peculiar abundances required for the isothermal models of the real *ASCA* data (Table 4) of all the galaxies also can be produced by forcing a isothermal model to fit the multiphase spectrum generated by the composite PSPC models. Although the PSPC models suggest the spectral properties of NGC 4636 are quite similar to the other galaxies, strong conclusions cannot be drawn from the radially varying isothermal models the PSPC data of NGC 4636 and NGC 4472 since they fail to produce the *ASCA* emission above  $\sim 3$  keV.

Therefore, our analysis of these systems demonstrates that isothermal models of the *ASCA* data within the  $r \sim 5'$  apertures are inconsistent with the *ASCA* and *ROSAT* PSPC data, a conclusion which cannot be attributed to reasonable errors in the MEKAL plasma code. Simple two-temperature and multiphase cooling flow models can provide good descriptions of these data sets with Fe abundances of  $\sim 1$ -2 solar and (except for NGC 4636) relative abundances fixed at their solar values (in good agreement with the results of BF); this situation is very analogous to that found for poor galaxy groups in a recent study (Buote 1999). Although the current data do not clearly distinguish between the two-temperature and cooling flow models, data will soon be available from the *Chandra*, *XMM*, and *ASTRO-E* satellites which can usefully address this issue (see section 6.3).

In section 6.2 we have discussed the implications of the approximately solar Fe abundances obtained for the multiphase models. The stellar abundances averaged over  $R_e$  computed by Arimoto et al. (1997) imply solar Fe abundances in agreement with the multiphase models. However, preliminary results reported in Loewenstein (1998) indicate the stellar Fe abundances are  $\sim 0.5$  solar. Using this smaller value we find that the standard chemical enrichment models of the hot gas in ellipticals (e.g. Ciotti et al. 1991) can reproduce the solar Fe abundance in the hot gas to within a factor of two. (This relatively small discrepancy essentially disappears if we increase the Fe abundances we have obtained by a factor of 1.44 to reflect the meteoritic solar abundances instead of the photospheric values we have used – see Ishimaru & Arimoto (1997).) Solar Fe abundances in the hot gas are also consistent with other enrichment models based on homogeneous (Brighenti & Mathews 1998b) and inhomogeneous cooling flows (Fujita et al. 1997).

Although the ellipticals in our sample are special in that they are among the brightest galaxies in relatively dense environments and have among the largest values of  $L_x/L_B$ , it is possible the evidence we have obtained for non-isothermal gas in these systems could be the result of their *ASCA* data

having perhaps the largest S/N among elliptical galaxies. If this is the case, the better quality data soon to become available should reveal that the hot gas in other ellipticals (at least near their centers) also consists of multiple temperature components with nearly solar Fe abundances.

## ACKNOWLEDGMENTS

It is a pleasure to thank W. Mathews, S. Faber, and G. Blumenthal for interesting discussions. Helpful comments and suggestions were provided by the anonymous referee and by the editor, A. Fabian. We also gratefully acknowledge K. Arnaud, K. Ebisawa, and others at the *ascahelp* and *rosathelp* email support services for their patient responses to questions regarding the *ASCA* and *ROSAT* data analysis software. The XSPEC implementation of the multiphase cooling flow model was kindly provided by R. Johnstone to whom we express our gratitude. This research has made use of *ASCA* data obtained from the High Energy Astrophysics Science Archive Research Center (HEASARC), provided by NASA's Goddard Space Flight Center. Support for this work was provided by NASA through Chandra Fellowship grant PF8-10001 awarded by the Chandra Science Center, which is operated by the Smithsonian Astrophysical Observatory for NASA under contract NAS8-39073.

## REFERENCES

- Anders E., Grevesse N., 1989, *Geochimica et Cosmochimica Acta*, 53, 197
- Arimoto N., Matsushita K., Ishimaru Y., Ohashi T., Renzini A., 1997, *ApJ*, 477, 128
- Arnaud K., 1996, in Jacoby G. and Barnes J., eds., *Astronomical Data Analysis Software and Systems V*, ASP Conf. Series volume 101, p17
- Arnaud, M., Rothenflug, R., 1985, *A&AS*, 60, 425
- Arnaud, M., Raymond, J., 1992, *ApJ*, 398, 394
- Awaki H., et al., 1994, *PASJ*, 46, L65
- Balucińska-Church M., McCammon D., 1992, 400, 699
- Brighenti F., Mathews W. G., 1998a, *ApJ*, 495, 239
- Brighenti F., Mathews W. G., 1998b, preprint
- Brown G. V., Beiersdorfer P., Liedahl D. A., Widmann K., Kahn S. M., 1998, *ApJ*, 502, 1015
- Buote D. A., 1999, *MNRAS*, submitted (astro-ph/9903278)
- Buote D. A., Canizares C. R., 1994, *ApJ*, 427, 86
- Buote D. A., Canizares C. R., 1997, *ApJ*, 474, 650
- Buote D. A., Fabian A. C., 1998, *MNRAS*, 296, 977 (BF)
- Buote D. A., Canizares C. R., Fabian A. C., 1998, *MNRAS*, submitted (astro-ph/9804290)
- Canizares C. R., Fabbiano G., Trinchieri G., 1987, *ApJ*, 312, 503
- Cappellaro E., Turatto M., Tsvetkov D. Yu., Bartunov O. S., Pollas C., Evans R., Hamuy M., *A&A*, 322, 431
- Ciotti L., D'Ercole A., Pellegrini S., Renzini A., 1991, *ApJ*, 376, 380
- David L. P., Jones C., Forman W., 1991, *ApJ*, 380, 39
- David L. P., Jones C., Forman W., Daines S., 1994, *ApJ*, 428, 544
- de Vaucouleurs G., de Vaucouleurs A., Corwin H.G., Buta R. J., Paturel G., Fouqué P., 1991, *Third Reference Catalogue of Bright Galaxies* (Austin: Univ. Texas Press) (RC3)
- Faber S. M., Wegner G., Burstein D., Davies R. L., Dressler A., Lynden-Bell D., Terlevich R. J., 1989, *ApJS*, 69, 763
- Fabian A. C., 1994, *ARA&A*, 32, 277
- Fabian A. C., Arnaud K. A., Bautz M. W., Tawara Y., 1994, *ApJ*, 436, L63

- Finoguenov A., Jones C., Forman W., David L., 1998, *ApJ*, in press (astro-ph/9810107)
- Forman W., Jones C., David L., Franx M., Makishima K., Ohashi T., 1993, *ApJ*, 418, L55
- Fujita Y., Fukumoto J., Okoshi K., 1997, *ApJ*, 488, 585
- Fukazawa Y., et al., 1996, *PASJ*, 48, 395
- Fukazawa Y., et al., 1998, *PASJ*, 50, 187
- Gendreau K., Yaqoob T., 1997, *ASCA XRT Calibration Issues*, in *ASCA News* vol. 5, (NASA/GSFC: Greenbelt)
- Hwang U., Mushotzky R. F., Loewenstein M., Markert T. H., Fukazawa Y., Matsumoto H., 1997, *ApJ*, 476, 560
- Irwin J. A., Sarazin C. L., 1996, *ApJ*, 471, 683
- Ishimaru Y., Arimoto N., 1997, *PASJ*, 49, 1
- Johnstone R. M., Fabian A. C., Edge A. C., Thomas P. A., 1992, *MNRAS*, 255, 431
- Jones C., Stern C., Forman W., Breen J., David L., Tucker W., Franx M., 1997, *ApJ*, 482, 143
- Kim D.-W., Fabbiano G., Trinchieri G., 1992, *ApJ*, 393, 134
- Kunieda H., et al., *XRT Status Report*, in *ASCA News* vol. 5, (NASA/GSFC: Greenbelt), 3
- Liedahl D. A., Osterheld A. L., Goldstein W. H., 1995, *ApJ*, 438, L115
- Loewenstein M., Mushotzky R. F., 1996, *ApJ*, 466, 695
- Loewenstein M., Mushotzky R. F., 1997, *Proceedings of IAU Symposium 187 on Cosmic Chemical Evolution*, in press (astro-ph/9710339)
- Loewenstein M., 1998, in eds. P. Carral and J. Cepa, *Star Formation in Early-Type Galaxies*, *ASP Conf. Ser.*, in press
- Matsumoto H., Koyama K., Awaki H., Tsuru T., Loewenstein M., Matsushita K., 1997, *ApJ*, 482, 133
- Matsushita K., et al., 1994, 436, L41
- Matsushita K., Makishima K., Rokutanda E., Yamasaki N., Ohashi T., 1997, *ApJ*, 488, L125
- Matsushita K., Makishima K., Ikebe Y., Rokutanda E., Yamasaki N., Ohashi T., 1998, *ApJ Letters*, in press
- Mewe R., Gronenschild E. H. B. M., van den Oord G. H. J., 1985, *A&AS*, 62, 197
- Orr A., Yaqoob T., Parmar A. N., Piro L., White N. E., Grandi P., 1998, *A&A*, 337, 685
- Pellegrini S., Ciotti L., 1998, *A&A*, 333, 433
- Rangarajan F. V. N., Fabian A. C., Forman W. R., Jones C., 1995, *MNRAS*, 272, 665
- Raymond J. C., Smith B. W., 1977, *ApJS*, 35, 419
- Stark A. A., Gammie C. F., Wilson R. W., Bally J., Linke R. A., Heiles C., Hurwitz M. 1992, *ApJS*, 79, 77
- Tanaka Y., Inoue H., & Holt S. S., 1994, *PASJ*, 46, L37
- Trinchieri G., Kim D.-W., Fabbiano G., Canizares C., 1994, *ApJ*, 428, 555
- Trümper J., 1983, *Adv. Space Res.*, 2, 241
- Wargelin B. J., Beiersdorfer P., Liedahl D. A., Kahn S. M., Von Goeler S., 1998, *ApJ*, 496, 1031
- Xu H., Makishima K., Fukazawa Y., Ikebe Y., Kikuchi K., Ohashi T., Tamura T., 1998, *ApJ*, 500, 738